

A High-Order Weighted Compact High Resolution Scheme with Boundary Closures for Compressible Turbulent Flows with Shocks

Akshay Subramaniam^{a,1}, Man Long Wong^{a,1}, Sanjiva K. Lele^{a,b,c}

^a*Department of Aeronautics & Astronautics, Stanford University, Stanford, CA 94305, USA*

^b*Department of Mechanical Engineering, Stanford University, Stanford, CA 94305, USA*

^c*Center for Turbulence Research, Stanford University, Stanford, CA 94305, USA*

Abstract

We present an improved high-order weighted compact high resolution (WCHR) scheme that extends the idea of weighted compact nonlinear schemes (WCNS's) using nonlinear interpolations in conjunction with compact finite difference schemes for shock-capturing in compressible turbulent flows. The proposed scheme has better resolution property than previous WCNS's. This is achieved by using a compact (or spatially implicit) form instead of the traditional fully explicit form for the nonlinear interpolation. Since compact interpolation schemes tend to have lower dispersion errors compared to explicit interpolation schemes, the proposed scheme has the ability to resolve more fine-scale features while still having the ability to provide sufficiently localized dissipation to capture shocks and discontinuities robustly. Approximate dispersion relation characteristics of this scheme are analyzed to show the superior resolution properties of the scheme compared to other WCNS's of similar orders of accuracy. Conservative and high-order accurate boundary schemes are also proposed for non-periodic problems. Further, a new conservative flux-difference form for compact finite difference schemes is derived and allows for the use of positivity-preserving limiters for improved robustness. Different test cases demonstrate the ability of this scheme to capture discontinuities in a robust and stable manner while also localizing the required numerical dissipation only to regions containing discontinuities and very high wavenumber features and hence preserving smooth flow features better in comparison to WCNS's.

Keywords: weighted compact nonlinear scheme (WCNS), weighted essentially non-oscillatory (WENO) interpolation, high-order, high-resolution, shock-capturing, boundary closure, compressible turbulence, localized dissipation, positivity-preserving

1. Introduction

Simulations of compressible flows that involve shock waves, contact discontinuities, and turbulence have conflicting requirements. While capturing discontinuities like shock

¹These authors contributed equally to the work.

waves, contact surfaces or vortex sheets require numerical dissipation for stabilization, the fine scales of turbulence are severely affected by numerical dissipation. Hence, a method that can adaptively switch between a low dissipation formulation in regions of smooth flow to a formulation that adds sufficient dissipation at discontinuities is of paramount importance. In the past, weighted essentially non-oscillatory (WENO) [23, 17, 30, 3, 19, 18] schemes, their variants weighted compact nonlinear schemes (WCNS's) [9, 36, 48, 29, 45] and targeted essentially non-oscillatory (TENO) [11] scheme have been proposed as methods to provide this adaptation. These schemes capture shocks well and improvements like the WENO6-CU-M2 [18] and WCNS6-LD [45] schemes localize the numerical dissipation to regions around discontinuities. However, their resolution properties are limited by the underlying explicit reconstruction and interpolation schemes. One way to improve the resolution of the adaptive scheme is to increase the stencil width of the scheme while optimizing the dispersion and dissipation properties under the constraint of same order of accuracy like the TENO scheme with tailored resolution by Fu et al. [12]. Another way for improved resolution is the use of compact or spatially implicit finite difference scheme. Lele [28] developed compact finite difference and interpolation schemes that are high order accurate and have spectral-like resolution properties. Although these schemes are well-suited for problems involving turbulence, they cannot be directly used for problems that contain sharp gradient features like shocks unless certain numerical regularization is used. One kind of numerical regularization for compact finite difference schemes is to add numerical dissipation explicitly [7, 8, 6, 2, 25, 40, 13, 44] in solutions to capture shocks and material interfaces using the localized artificial diffusivity (LAD) first proposed by Cook and Cabot [8]. These regularization methods preserve the resolution properties of compact schemes, but are still prone to some mild spurious oscillations near shocks or discontinuities. They also, in some cases, introduce additional time step limitations due to the extra artificial dissipation terms. In addition to adding dissipation terms, solutions typically need to be filtered at every time step for de-aliasing.

As an alternative to adding artificial dissipation explicitly, Deng and Zhang [9] used a compact finite difference scheme with WENO interpolation in the context of WCNS. The process in obtaining flux at midpoints using nonlinear interpolations can be interpreted as a nonlinear filtering process to prevent spurious oscillations near discontinuities. However, the fact that WENO interpolation is explicit limits the effective resolution of the overall scheme even though compact finite difference scheme is used. Ghosh and Baeder [14] developed an upwind-biased compact reconstruction WENO scheme called CRWENO. This method is purely compact, but the scheme is upwind-biased and excessively damps the fine scales of turbulence.

In this paper, we present a newly designed scheme that is based on the WCNS formalism to use a compact finite difference derivative but is also improved with the use of a high-resolution compact nonlinear interpolation scheme. The localized dissipation (LD) nonlinear weights of Wong and Lele [45] are used to provide localized dissipation through adaptive switching between explicit and compact interpolations. Boundary interpolation and derivative schemes are also provided for non-periodic problems. The boundary schemes are conservative, have the same formal order of accuracy as in the interior schemes and are optimized by matching their truncation errors to the interior schemes. The overall improved scheme is shown to have better resolution properties than WCNS's using only explicit interpolations and is also stable and accurate for problems involving inflow-outflow boundaries with significant disturbances when proper boundary

treatments are applied.

2. Numerical methods

In this section, a scalar conservation law of the following form is considered in a one-dimensional (1D) domain of size $x \in [x_a, x_b]$ for simplicity:

$$\frac{\partial u}{\partial t} + \frac{\partial F(u)}{\partial x} = 0, \quad (1)$$

where $u(x, t)$ is a conserved scalar quantity that depends on space x and time t and $F(u)$ is a flux function of u . The equation above is discretized on a uniform grid with N cells and the solution u on the cell node at position $x_j = x_a + (j + 1/2)\Delta x$ is denoted by u_j , $\forall j \in \{0, 1, \dots, N-1\}$, where $\Delta x = (x_b - x_a)/N$. The cell midpoints are indexed by half integer values $x_{j+\frac{1}{2}}$, $\forall j \in \{-1, 0, 1, \dots, N-1\}$. The numerical method described in this section can be easily extended to two-dimensional (2D) and three-dimensional (3D) problems using the method of lines. The extension of the scalar conservation equation to a hyperbolic system of coupled equations such as the Euler equations is discussed in section 2.6.

2.1. Compact and explicit finite difference schemes

Over the years, various forms of finite difference schemes have been used in WCNS's to obtain the flux derivative in equation (1). Deng and Zhang [9] first used the sixth order compact midpoint-to-node finite difference (CMD) scheme by Lele [28] in following form:

$$\frac{9}{80}\hat{F}'_{j-1} + \frac{31}{40}\hat{F}'_j + \frac{9}{80}\hat{F}'_{j+1} = \frac{1}{\Delta x} \left[\frac{63}{80} \left(\tilde{F}_{j+\frac{1}{2}} - \tilde{F}_{j-\frac{1}{2}} \right) + \frac{17}{240} \left(\tilde{F}_{j+\frac{3}{2}} - \tilde{F}_{j-\frac{3}{2}} \right) \right], \quad (2)$$

where \hat{F}'_j are numerically approximated first derivatives of flux at cell nodes and $\tilde{F}_{j+\frac{1}{2}}$ are interpolated fluxes at cell midpoints. Since the resolution properties of WCNS's are mainly dominated by the nonlinear interpolations, Nonomura and Fujii [34] suggested using a more efficient explicit sixth order midpoint-to-node finite difference (MD) scheme:

$$\hat{F}'_j = \frac{1}{\Delta x} \left[\frac{75}{64} \left(\tilde{F}_{j+\frac{1}{2}} - \tilde{F}_{j-\frac{1}{2}} \right) - \frac{25}{384} \left(\tilde{F}_{j+\frac{3}{2}} - \tilde{F}_{j-\frac{3}{2}} \right) + \frac{3}{640} \left(\tilde{F}_{j+\frac{5}{2}} - \tilde{F}_{j-\frac{5}{2}} \right) \right]. \quad (3)$$

Nonomura and Fujii [35] later also proposed a robust explicit sixth order midpoint-and-node-to-node finite difference (MND) scheme:

$$\hat{F}'_j = \frac{1}{\Delta x} \left[\frac{3}{2} \left(\tilde{F}_{j+\frac{1}{2}} - \tilde{F}_{j-\frac{1}{2}} \right) - \frac{3}{10} (F_{j+1} - F_{j-1}) - \frac{25}{384} \left(\tilde{F}_{j+\frac{3}{2}} - \tilde{F}_{j-\frac{3}{2}} \right) \right], \quad (4)$$

where F_j are fluxes at cell nodes².

²Equation (4) uses F_{j-1} and F_{j+1} instead of \tilde{F}_{j-1} and \tilde{F}_{j+1} since the fluxes at nodes can be directly evaluated from the conservative variables at nodes and require no interpolation.

2.2. Weighted compact nonlinear schemes (WCNS's)

In WCNS's, the fluxes at the cell midpoints are obtained with aid of explicit nonlinear interpolations, which can also be interpreted as a nonlinear filtering processes to avoid spurious oscillations near shocks and other discontinuities. For the scalar conservation equation (1), the algorithm to obtain the flux derivative with WCNS's is given below:

1. Compute a left-biased and a right-biased interpolated solution value \tilde{u}_L and \tilde{u}_R at each cell midpoint using explicit nonlinear interpolations.
2. Compute the flux at the cell midpoints using a flux difference splitting method $\tilde{F}_{j+\frac{1}{2}} = F_{\text{split}}(\tilde{u}_L, \tilde{u}_R)$ (typically a Riemann solver).
3. Compute the flux at the cell nodes $F_j = F(u_j)$ if the node values of flux are needed in the finite difference scheme e.g. MND scheme in equation (4).
4. Use the flux(es) $\tilde{F}_{j+\frac{1}{2}}$ (and F_j) to compute the flux derivative F'_j with a compact or explicit central finite difference scheme.

In this work, only the interpolations of left-biased cell midpoint values are presented. The interpolations of right-biased cell midpoint values are similar due to symmetry and can be obtained by flipping the stencils and corresponding coefficients. It should also be noted that flux vector splitting methods such as Lax–Friedrichs flux splitting can also be used in WCNS's where the flux values are interpolated instead of the solution values, but that is not the procedure followed in this paper.

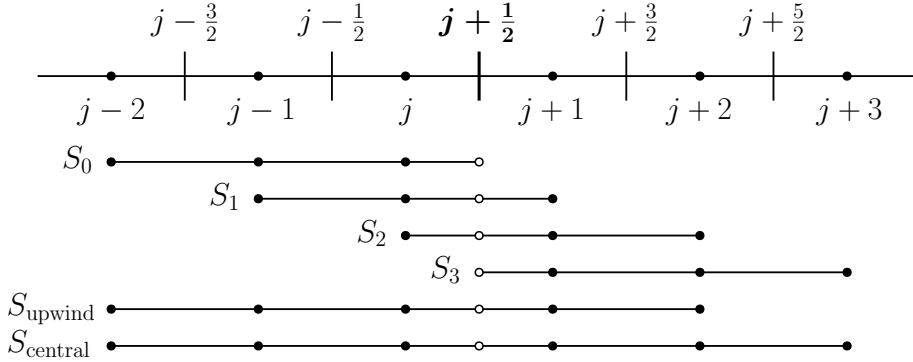


Figure 1: Sub-stencils of WCNS's. The solid circles represent points used in the right hand side of the interpolation stencils, while empty circles represent points used in the left hand side of the interpolation stencils.

Despite the robustness of interpolations using upwind-biased nonlinear weights in capturing shocks like those by Jiang and Shu [23] (JS) and that by Borges et al. [3] (Z), they are excessively dissipative in smooth regions. To remedy this, Martín et al. [30], Hu et al. [19] proposed a nonlinear interpolation that minimizes dissipation in smooth regions by including the downwind stencil, S_3 in figure 1. Wong and Lele [45] further optimized the nonlinear weighting procedure by proposing a localized dissipative (LD) interpolation. The LD interpolation approximates the midpoint values by computing third order linear interpolated values from four different sub-stencils, $S_0 - S_3$ (shown in figure 1) and then taking a nonlinear combination of these four values. The interpolated values at the

midpoints $\tilde{u}_{j+\frac{1}{2}}$ from the four different explicit interpolations³ (EI_k) are given by:

$$EI_0 : \quad \tilde{u}_{j+\frac{1}{2}}^{(0)} = \frac{1}{8} (3u_{j-2} - 10u_{j-1} + 15u_j), \quad (5)$$

$$EI_1 : \quad \tilde{u}_{j+\frac{1}{2}}^{(1)} = \frac{1}{8} (-u_{j-1} + 6u_j + 3u_{j+1}), \quad (6)$$

$$EI_2 : \quad \tilde{u}_{j+\frac{1}{2}}^{(2)} = \frac{1}{8} (3u_j + 6u_{j+1} - u_{j+2}), \quad (7)$$

$$EI_3 : \quad \tilde{u}_{j+\frac{1}{2}}^{(3)} = \frac{1}{8} (15u_{j+1} - 10u_{j+2} + 3u_{j+3}). \quad (8)$$

The fifth order linear upwind-biased interpolation EI_{upwind} and sixth order linear central interpolation EI_{central} from S_{upwind} and S_{central} in figure 1 respectively can be obtained from linear combinations of the third order interpolations:

$$EI_{\text{upwind}} = \sum_{k=0}^2 d_k^{\text{upwind}} EI_k, \quad (9)$$

$$EI_{\text{central}} = \sum_{k=0}^3 d_k^{\text{central}} EI_k, \quad (10)$$

where the linear weights are given by:

$$d_0^{\text{upwind}} = \frac{1}{16}, \quad d_1^{\text{upwind}} = \frac{10}{16}, \quad d_2^{\text{upwind}} = \frac{5}{16}, \quad (11)$$

$$d_0^{\text{central}} = \frac{1}{32}, \quad d_1^{\text{central}} = \frac{15}{32}, \quad d_2^{\text{central}} = \frac{15}{32}, \quad d_3^{\text{central}} = \frac{1}{32}. \quad (12)$$

The expanded form of the linear interpolations from S_{upwind} and S_{central} are given by:

$$EI_{\text{upwind}} : \quad \tilde{u}_{j+\frac{1}{2}}^{\text{upwind}} = \frac{1}{128} (3u_{j-2} - 20u_{j-1} + 90u_j + 60u_{j+1} - 5u_{j+2}), \quad (13)$$

$$EI_{\text{central}} : \quad \tilde{u}_{j+\frac{1}{2}}^{\text{central}} = \frac{1}{256} (3u_{j-2} - 25u_{j-1} + 150u_j + 150u_{j+1} - 25u_{j+2} + 3u_{j+3}). \quad (14)$$

The nonlinear LD interpolation is formulated by replacing the linear weights d_k^{central} in equation (10) with nonlinear weights ω_k as:

$$\tilde{u}_{j+\frac{1}{2}} = \sum_{k=0}^3 \omega_k \tilde{u}_{j+\frac{1}{2}}^{(k)}. \quad (15)$$

In smooth regions, the interpolated value given by LD interpolation should converge to the value given by the sixth order linear central interpolation in equation (14). The forms

³Technically, EI_0 and EI_3 are extrapolations and not interpolations, but we call them interpolations anyway in order to simplify the terminology.

of nonlinear weights of the LD interpolation, as well as those of JS and Z interpolations are given in [Appendix A](#).

The CMD scheme (equation (2)) in conjunction with JS, Z, and LD interpolations are called WCNS5-JS, WCNS5-Z, and WCNS6-LD, respectively. The MND scheme (equation (4)) in conjunction with the three different interpolations are called MND-WCNS5-JS, MND-WCNS5-Z, and MND-WCNS6-LD. The numbers in the names indicate the formal orders of accuracy of the schemes. The difference between the three nonlinear interpolation methods is discussed in Wong and Lele [45].

2.3. Weighted compact high resolution (WCHR) scheme

2.3.1. Explicit-compact interpolation (ECI)

WCNS's use explicit interpolations, which typically have larger errors in the real part of the transfer function compared to compact interpolations of the same order of accuracy. In the context of a linear advection equation, this error in the real part of the transfer function manifests itself as a dispersion error. In this sub-section, we propose a new nonlinear explicit-compact interpolation that minimizes the dispersion error by adaptively switching to linear compact interpolations in smooth regions.

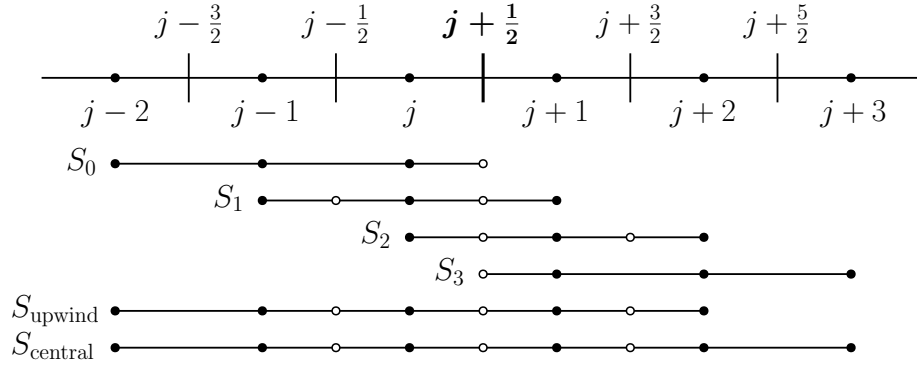


Figure 2: Sub-stencils of the WCHR6 scheme. The solid circles represent points used in the right hand side of the interpolation stencils, while empty circles represent points used in the left hand side of the interpolation stencils.

Instead of using only explicit interpolations in sub-stencils, the interpolation methods in the central two sub-stencils in figure 1 are replaced with compact interpolations. In smooth regions where all the four stencils are used, the interpolation becomes compact and has better resolution properties while near discontinuities where the most left or right biased stencil is used, the interpolation reverts to being explicit for robustness. The interpolation methods (ECI_k) in the sub-stencils $S_0 - S_3$ of figure 2 are given by:

$$ECI_0 : \quad \tilde{u}_{j+\frac{1}{2}}^{(0)} = \frac{3}{8}u_{j-2} - \frac{5}{4}u_{j-1} + \frac{15}{8}u_j, \quad (16)$$

$$ECI_1 : \quad -(\xi - 1)\tilde{u}_{j-\frac{1}{2}}^{(1)} + \xi\tilde{u}_{j+\frac{1}{2}}^{(1)} = -\frac{4\xi - 3}{8}u_{j-1} + \frac{3}{4}u_j + \frac{4\xi - 1}{8}u_{j+1}, \quad (17)$$

$$ECI_2 : \quad \xi\tilde{u}_{j+\frac{1}{2}}^{(2)} - (\xi - 1)\tilde{u}_{j+\frac{3}{2}}^{(2)} = \frac{4\xi - 1}{8}u_j + \frac{3}{4}u_{j+1} - \frac{4\xi - 3}{8}u_{j+2}, \quad (18)$$

$$ECI_3 : \quad \tilde{u}_{j+\frac{1}{2}}^{(3)} = \frac{15}{8}u_{j+1} - \frac{5}{4}u_{j+2} + \frac{3}{8}u_{j+3}, \quad (19)$$

where ξ is a free parameter that can be used to control the dispersion and dissipation characteristics of the scheme. When $\xi = 1$, the explicit-compact interpolations reduce to fully explicit interpolations. In general, S_1 and S_2 in equations (17) - (18) are third order accurate except for $\xi = 5/8$ when they both become fourth order accurate.

The fifth order linear upwind-biased and sixth order linear central interpolations from S_{upwind} and S_{central} in figure 2 respectively can be obtained from linear combinations of the third order interpolations:

$$ECI_{\text{upwind}} = \sum_{k=0}^2 d_k^{\text{upwind}} ECI_k, \quad (20)$$

$$ECI_{\text{central}} = \sum_{k=0}^3 d_k^{\text{central}} ECI_k, \quad (21)$$

where the linear weights are given by:

$$d_0^{\text{upwind}} = \frac{8\xi - 5}{8(\xi + 5)}, \quad d_1^{\text{upwind}} = \frac{5(13\xi - 7)}{8(\xi + 5)(2\xi - 1)}, \quad d_2^{\text{upwind}} = \frac{5(5\xi - 2)}{8(\xi + 5)(2\xi - 1)}, \quad (22)$$

$$d_0^{\text{central}} = \frac{8\xi - 5}{16(\xi + 5)}, \quad d_1^{\text{central}} = \frac{45}{16(\xi + 5)}, \quad d_2^{\text{central}} = \frac{45}{16(\xi + 5)}, \quad d_3^{\text{central}} = \frac{8\xi - 5}{16(\xi + 5)}. \quad (23)$$

Note that the linear weights for explicit-compact interpolations are in general different from those for explicit interpolations except when $\xi = 1$. The expanded form of the linear interpolations from S_{upwind} and S_{central} are given by:

$$ECI_{\text{upwind}} : \quad \alpha^{\text{upwind}}\tilde{u}_{j-\frac{1}{2}}^{\text{upwind}} + \beta^{\text{upwind}}\tilde{u}_{j+\frac{1}{2}}^{\text{upwind}} + \gamma^{\text{upwind}}\tilde{u}_{j+\frac{3}{2}}^{\text{upwind}} = a^{\text{upwind}}u_{j-2} + b^{\text{upwind}}u_{j-1} + c^{\text{upwind}}u_j + d^{\text{upwind}}u_{j+1} + e^{\text{upwind}}u_{j+2}, \quad (24)$$

$$ECI_{\text{central}} : \quad \alpha^{\text{central}}\tilde{u}_{j-\frac{1}{2}}^{\text{central}} + \beta^{\text{central}}\tilde{u}_{j+\frac{1}{2}}^{\text{central}} + \gamma^{\text{central}}\tilde{u}_{j+\frac{3}{2}}^{\text{central}} = a^{\text{central}}u_{j-2} + b^{\text{central}}u_{j-1} + c^{\text{central}}u_j + d^{\text{central}}u_{j+1} + e^{\text{central}}u_{j+2} + f^{\text{central}}u_{j+3}. \quad (25)$$

The coefficients in equations (24) and (25) are given in Appendix B.1.

Figure 3 shows the relations between the linear weights of the most upwind stencil S_0 in ECI_{upwind} and ECI_{central} and ξ . For both linear weights to be positive, ξ has to be larger than $5/8$. For increasing $\xi > 5/8$, the linear weights for the most upwind stencil increase linearly.

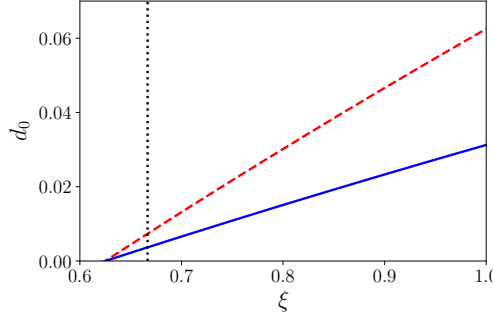


Figure 3: Linear weights of sub-stencil S_0 of ECI_{upwind} and ECI_{central} against ξ . Red dashed line: ECI_{upwind} ; blue solid line: ECI_{central} . The black dotted vertical line indicates $\xi = 2/3$ which is chosen for both ECI's in this work.

Even when used with a perfect derivative scheme, the interpolation transfer function creates dispersion and dissipation errors in a linear advection problem. Figures 4 and 5 show the modified wavenumber of ECI_{upwind} and ECI_{central} respectively when used with an analytical derivative scheme. When ξ is decreased from 1 to $5/8$, the resolution increases in both ECI's and the dissipation of ECI_{upwind} decreases. It should be noted that the dissipation error of ECI_{central} is always zero independent of value of ξ and the dispersion errors of both ECI_{upwind} and ECI_{central} are the same when $\xi = 5/8$ as both of them become identical. We use a value of $\xi = 2/3$ in this paper. This value of ξ is chosen based on the dispersion relations of the linear schemes as a balance between high resolution and robustness. More rigorous optimization procedures may be used to choose an optimal value of ξ but that is left to future work.

2.3.2. Weighted compact high resolution (WCHR) scheme

The finite difference schemes described in section 2.1 may generate spurious oscillations due to Gibbs phenomenon or even be unstable near shocks or discontinuities with either ECI_{upwind} or ECI_{central} . Hence, we use a nonlinear combination of the sub-stencil interpolations with the LD nonlinear weights in equation (A.9) at any midpoint:

$$ECI_{\text{nonlinear}} = \sum_{k=0}^3 \omega_k ECI_k. \quad (26)$$

The CMD scheme in equation (2) with the nonlinear explicit-compact interpolation ($ECI_{\text{nonlinear}}$) is sixth order accurate in smooth regions and is called weighted compact high resolution scheme, WCHR6, in this paper due to its high resolution property compared to other WCNS's.

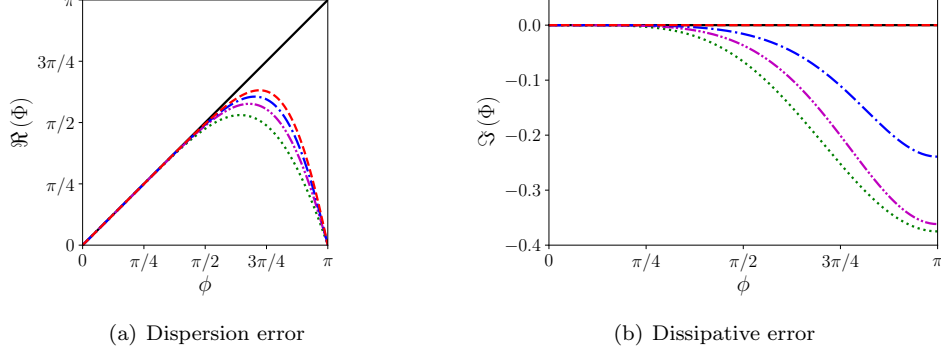


Figure 4: Modified reduced wavenumber, Φ , against reduced wavenumber, ϕ , of ECI_{upwind} . Black solid line: exact; green dotted line: $\xi = 1$; magenta dashed-dotted-dotted line: $\xi = 3/4$; blue dashed-dotted line: $\xi = 2/3$; red dashed line: $\xi = 5/8$.

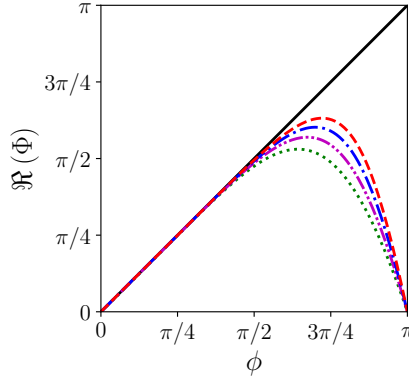


Figure 5: Real part of modified reduced wavenumber, Φ , against reduced wavenumber, ϕ , of ECI_{central} representing dispersion error. Black solid line: exact; green dotted line: $\xi = 1$; magenta dashed-dotted-dotted line: $\xi = 3/4$; blue dash-dotted line: $\xi = 2/3$; red dashed line: $\xi = 5/8$.

The parameters for computing the nonlinear weights in WCNS's and WCHR6 scheme are discussed in [Appendix A](#). The parameter values of each scheme in this work are given in [table 1](#). For a discussion on the choice of parameters in LD nonlinear weights, see [\[45\]](#). The parameters used here for WCHR6 provide stable results while preserving the high resolution property of the underlying compact interpolation scheme. They are also chosen so that numerical dissipation is only locally added to regions containing discontinuities and have minimal effect on regions where the solution is smooth.

2.4. Approximate dispersion relation

For linear schemes, the dissipation and dispersion characteristics can be determined using a dispersion relation analysis discussed by Lele [\[28\]](#). However, this analysis can-

Numerical schemes	Parameter values				
	p	q	C	α_{RL}^τ	ξ
WCNS5-JS	2	—	—	—	—
WCNS5-Z	2	—	—	—	—
WCNS6-LD	2	4	1.0e9	35.0	—
WCHR6	2	4	1.0e10	55.0	2/3

Table 1: Parameters for different numerical schemes.

not be used for nonlinear schemes. Pirozzoli [37] developed an approximate dispersion relation (ADR) technique to characterize the dispersion and dissipation characteristics of general nonlinear schemes. Results from ADR analysis are shown in figure 6 for the WCHR6 scheme and WCNS's using compact (CMD) and explicit (MND) derivatives. In figure 6(a) where the dispersion characteristics are shown, we can see that the WCHR6 scheme outperforms other schemes in dispersion error. Explicit nonlinear interpolations with CMD in general have higher resolution than those with MND. Figure 7 shows the dispersion errors for WCHR6 and the WCNS's with explicit interpolations and compact derivative (CMD) on a semi-log plot. Given a threshold ϵ_{res} for the maximum tolerable dispersion error, a resolving efficiency of the different schemes can be computed. The resolving efficiency is defined as the fraction of Nyquist wavenumber that the scheme can resolve within the given dispersion error tolerance ϵ_{res} . In figure 7, the horizontal black dashed line represents $\epsilon_{\text{res}} = 0.01$ and the vertical colored dashed lines represent the maximum wavenumber that each scheme can resolve given this threshold. Table 2 shows the resolving efficiency for the four different schemes. From the plot, it can be seen that the WCHR6 has much higher resolution ability compared to other schemes of similar orders of accuracy ($\sim 45.8\%$ more than the WCNS5-JS). All schemes considered in figure 7 use CMD as the flux derivative. This clearly shows the benefit of using compact interpolation to achieve better resolution characteristics. Figure 6(b) shows the dissipation characteristics of the schemes. In the plot, we see that WCNS5-JS and WCNS5-Z have dissipation over a wide range of wavenumbers while WCNS6-LD has much more localized dissipation only in high wavenumber range. Due to the high resolution characteristic of WCHR6, we choose the parameters in the LD weights such that it has more localized dissipation than WCNS6-LD in the wavenumber space. The high resolution and localized dissipation characteristics of WCHR6 are especially important for problems involving turbulence transition where low resolution and excessive dissipation can curtail the range of scales in the problem.

2.5. Boundary closures

Boundary schemes are essential for interpolation and numerical derivative at the domain boundaries. In this section, we present boundary schemes for both interpolation and conservative derivative that preserve the order of accuracy and have truncation errors matched to those of the interior schemes. The boundary schemes presented here use ghost points at domain boundaries. Specific algorithms to evaluate function values for the ghost points are described in section 3.

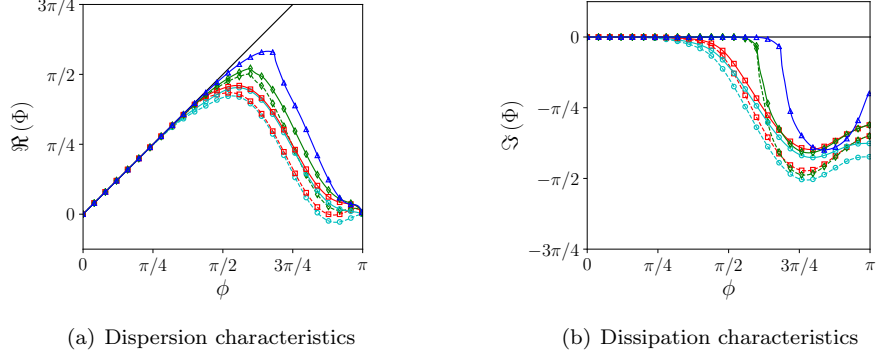


Figure 6: ADR's of different numerical schemes. Black solid line: spectral; dashed line with cyan circles: MND-WCNS5-JS; solid line with cyan circles: WCNS5-JS; dashed line with red squares: MND-WCNS5-Z; solid line with red squares: WCNS5-Z; dashed line with green diamonds: MND-WCNS6-LD; solid line with green diamonds: WCNS6-LD; solid line with blue triangles: WCHR6.

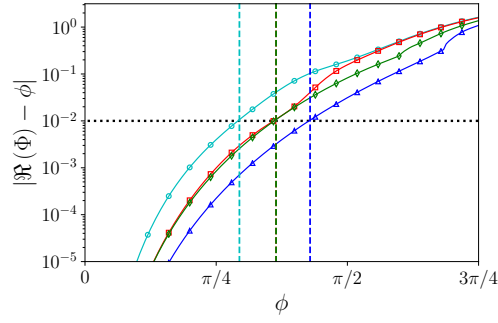


Figure 7: Approximate dispersion errors (derivation of real part of modified reduced wavenumber from that of reduced wavenumber) of different numerical schemes. Cyan circles: WCNS5-JS; red squares: WCNS5-Z; green diamonds: WCNS6-LD; blue triangles: WCHR6.

Numerical schemes	Resolving efficiency	Improvement over WCNS5-JS
WCNS5-JS	0.294	—
WCNS5-Z	0.364	23.7%
WCNS6-LD	0.364	23.7%
WCHR6	0.429	45.8%

Table 2: Resolving efficiency of different schemes for $\epsilon_{\text{res}} = 0.01$.

2.5.1. Interpolations

Only left-biased interpolations at the left boundary (LB) and right boundary (RB) are discussed in this section. The right-biased interpolations at the left and right boundaries are simply the mirror images of the left-biased interpolations at the right and left boundaries respectively. The sub-stencils of the left-biased interpolation scheme at LB is shown in figure 8.

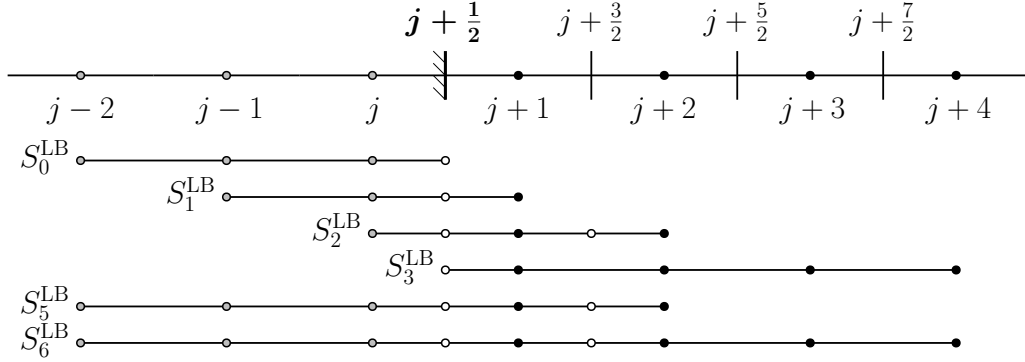


Figure 8: Sub-stencils of the left-biased interpolation scheme at the left boundary (LB). The solid and gray circles represent points used in the right hand side of the compact interpolation stencils, while empty circles represent points used in the left hand side of the interpolation stencils. The solid and gray circles represent the interior points and ghost points respectively.

The four third order interpolations from S_0^{LB} - S_3^{LB} in figure 8 are given by:

$$ECI_0^{\text{LB}} : \quad \tilde{u}_{j+\frac{1}{2}}^{(0)} = \frac{3}{8}u_{j-2} - \frac{5}{4}u_{j-1} + \frac{15}{8}u_j, \quad (27)$$

$$ECI_1^{\text{LB}} : \quad \tilde{u}_{j+\frac{1}{2}}^{(1)} = -\frac{1}{8}u_{j-1} + \frac{3}{4}u_j + \frac{3}{8}u_{j+1}, \quad (28)$$

$$ECI_2^{\text{LB}} : \quad a^{\text{LB}}\tilde{u}_{j+\frac{1}{2}}^{(2)} + b^{\text{LB}}\tilde{u}_{j+\frac{3}{2}}^{(2)} = c^{\text{LB}}u_j + d^{\text{LB}}u_{j+1} + e^{\text{LB}}u_{j+2}, \quad (29)$$

$$ECI_3^{\text{LB}} : \quad \tilde{u}_{j+\frac{1}{2}}^{(3)} = f^{\text{LB}}u_{j+1} + g^{\text{LB}}u_{j+2} + h^{\text{LB}}u_{j+3} + i^{\text{LB}}u_{j+4}. \quad (30)$$

The fifth order and sixth order linear interpolations from S_5^{LB} and S_6^{LB} in figure 8 respectively can be obtained from linear combinations of the third order interpolations:

$$ECI_5^{\text{LB}} = \sum_{k=0}^2 d_k^{(5),\text{LB}} ECI_k^{\text{LB}}, \quad (31)$$

$$ECI_6^{\text{LB}} = \sum_{k=0}^3 d_k^{(6),\text{LB}} ECI_k^{\text{LB}}. \quad (32)$$

The sub-stencils of the left-biased interpolation scheme at RB is shown in figure 9. The four third order interpolations from S_0^{RB} - S_3^{RB} in figure 9 are given by:

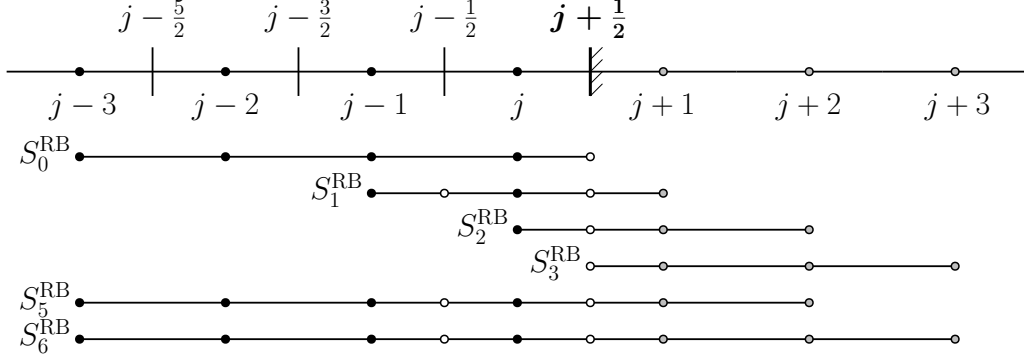


Figure 9: Sub-stencils of the left-biased interpolation scheme at the right boundary (RB). The solid and gray circles represent points used in the right hand side of the compact interpolation stencils, while empty circles represent points used in the left hand side of the interpolation stencils. The solid and gray circles represent the interior points and ghost points respectively.

$$ECI_0^{\text{RB}} : \quad \tilde{u}_{j+\frac{1}{2}}^{(0)} = a^{\text{RB}} u_{j-3} + b^{\text{RB}} u_{j-2} + c^{\text{RB}} u_{j-1} + d^{\text{RB}} u_j, \quad (33)$$

$$ECI_1^{\text{RB}} : \quad e^{\text{RB}} \tilde{u}_{j-\frac{1}{2}}^{(1)} + f^{\text{RB}} \tilde{u}_{j+\frac{1}{2}}^{(1)} = g^{\text{RB}} u_{j-1} + h^{\text{RB}} u_j + i^{\text{RB}} u_{j+1}, \quad (34)$$

$$ECI_2^{\text{RB}} : \quad \tilde{u}_{j+\frac{1}{2}}^{(2)} = \frac{3}{8} u_j + \frac{3}{4} u_{j+1} - \frac{1}{8} u_{j+2}, \quad (35)$$

$$ECI_3^{\text{RB}} : \quad \tilde{u}_{j+\frac{1}{2}}^{(3)} = \frac{15}{8} u_{j+1} - \frac{5}{4} u_{j+2} + \frac{3}{8} u_{j+3}. \quad (36)$$

The fifth order and sixth order linear interpolations from S_5^{RB} and S_6^{RB} in figure 9 respectively can be obtained from linear combinations of the third order interpolations:

$$ECI_5^{\text{RB}} = \sum_{k=0}^2 d_k^{(5),\text{RB}} ECI_k^{\text{RB}}, \quad (37)$$

$$ECI_6^{\text{RB}} = \sum_{k=0}^3 d_k^{(6),\text{RB}} ECI_k^{\text{RB}}. \quad (38)$$

The coefficients in the sub-stencils and the linear weights of the interpolation schemes at the LB and RB are given in [Appendix B.2](#). There are two free parameters for each of the boundary interpolation scheme. The free parameters are set such that the first nonzero truncation errors of $ECI_5^{\text{LB}}/ECI_5^{\text{RB}}$ and $ECI_6^{\text{LB}}/ECI_6^{\text{RB}}$ match those of ECI_{upwind} and ECI_{central} of equations (24) and (25) respectively. To capture discontinuities, the linear weights are replaced with the LD nonlinear weights in [Appendix A.3](#).

2.5.2. Derivatives

A derivative boundary closure for an interior scheme given in equation (2) is only required at the last boundary point. The boundary derivative schemes at the boundary points are derived by using flux difference formulations of compact finite difference

schemes and enforcing discrete conservation. It is proved in [Appendix D](#) that any compact or explicit central finite difference scheme can be rewritten in the flux difference form given by:

$$\left. \frac{\partial \widehat{F}}{\partial x} \right|_{x=x_j} = \widehat{F}'_j = \frac{1}{\Delta x} \left(\widehat{F}_{j+\frac{1}{2}} - \widehat{F}_{j-\frac{1}{2}} \right), \quad (39)$$

where $\widehat{F}_{j+\frac{1}{2}}$ are the reconstructed fluxes at midpoints. $\widehat{F}_{j+\frac{1}{2}}$ of the sixth order CMD (equation (2)) are given by:

$$\frac{9}{80} \widehat{F}_{j-\frac{1}{2}} + \frac{31}{40} \widehat{F}_{j+\frac{1}{2}} + \frac{9}{80} \widehat{F}_{j+\frac{3}{2}} = \frac{17}{240} F_{j-\frac{1}{2}} + \frac{103}{120} F_{j+\frac{1}{2}} + \frac{17}{240} F_{j+\frac{3}{2}}. \quad (40)$$

In deriving the boundary closure for the CMD derivative scheme, we seek for a closure for the flux reconstruction equation such that the truncation error of the boundary derivative scheme is matched to that of the interior derivative scheme up to seventh order. This gives the following boundary scheme at the left boundary with $j = 0$:

$$\begin{aligned} \frac{31}{40} \widehat{F}'_j + \frac{9}{80} \widehat{F}'_{j+1} = \frac{1}{\Delta x} & \left[\frac{1633}{5376000} F_{j-2} + \frac{9007}{192000} F_{j-1} - \frac{29567}{48000} \tilde{F}_{j-\frac{1}{2}} - \frac{65699}{76800} F_j \right. \\ & \left. + \frac{44033}{24000} \tilde{F}_{j+\frac{1}{2}} - \frac{26353}{38400} F_{j+1} + \frac{104579}{336000} \tilde{F}_{j+\frac{3}{2}} - \frac{27233}{768000} F_{j+2} \right]. \end{aligned} \quad (41)$$

The derivative scheme for the right boundary at $j = N - 1$ can be obtained by mirroring the above derivative scheme:

$$\begin{aligned} \frac{9}{80} \widehat{F}'_{j-1} + \frac{31}{40} \widehat{F}'_j = \frac{1}{\Delta x} & \left[\frac{27233}{768000} F_{j-2} - \frac{104579}{336000} \tilde{F}_{j-\frac{3}{2}} + \frac{26353}{38400} F_{j-1} - \frac{44033}{24000} \tilde{F}_{j-\frac{1}{2}} \right. \\ & \left. + \frac{65699}{76800} F_j + \frac{29567}{48000} \tilde{F}_{j+\frac{1}{2}} - \frac{9007}{192000} F_{j+1} - \frac{1633}{5376000} F_{j+2} \right]. \end{aligned} \quad (42)$$

The relation between finite difference schemes and their flux difference forms, and the details on how to derive the boundary schemes with the flux difference form are further discussed in [Appendix D](#).

2.6. Extension to Euler equations

The inviscid 1D Euler equations are given by:

$$\frac{\partial \mathbf{Q}}{\partial t} + \frac{\partial \mathbf{F}(\mathbf{Q})}{\partial x} = 0, \quad (43)$$

where

$$\mathbf{Q} = \begin{pmatrix} \rho \\ \rho u \\ E \end{pmatrix} \quad \text{and} \quad \mathbf{F}(\mathbf{Q}) = \begin{pmatrix} \rho u \\ \rho u^2 + p \\ (E + p) u \end{pmatrix}, \quad (44)$$

where ρ is the density, u is the velocity, E is the total energy, and $p = (\gamma - 1) (E - \rho u^2 / 2)$ is the pressure.

The WCNS's or WCHR6 scheme can be applied to the Euler equations in a similar fashion as the scalar conservation law. Equations (2), (3), and (4) can be used to get

the flux derivatives based on the fluxes at the nodes \mathbf{F}_j and the fluxes at the midpoints $\tilde{\mathbf{F}}_{j+\frac{1}{2}} = \mathbf{F}_{\text{Riemann}}(\tilde{\mathbf{Q}}_L, \tilde{\mathbf{Q}}_R)$ where $\tilde{\mathbf{Q}}_L$ and $\tilde{\mathbf{Q}}_R$ are the left and right interpolated solution vectors at the midpoints and $\mathbf{F}_{\text{Riemann}}$ are the fluxes from a Riemann solver. In this work, the HLLC Riemann solver is used (see [Appendix E](#) for details on the Riemann solver) for 1D problems. Although the interpolated solution vectors at the midpoints can be computed by directly interpolating the conserved variables or the primitive variables (ρ, u, p) using the weighted interpolations, it was found that projecting variables to the local characteristic fields before reconstruction and interpolation can improve the numerical stability at discontinuities. By exploiting the fact that the equations are decoupled in the characteristic space, numerical dissipation is added much more precisely at shocks. The characteristic decomposition and interpolation with the WCHR6 scheme is described in the section below.

2.6.1. Characteristic decomposition

For the 1D Euler equation system in primitive form, the three characteristic variables, ξ^0 , ξ^1 , and ξ^2 , at midpoint are given by:

$$\begin{pmatrix} \xi^0 \\ \xi^1 \\ \xi^2 \end{pmatrix} = \mathbf{R}^{-1} \begin{pmatrix} \rho \\ u \\ p \end{pmatrix}, \quad (45)$$

where \mathbf{R}^{-1} is the matrix of the left eigenvectors (inverse of the matrix of the right eigenvectors \mathbf{R}) of the linearized Euler system given by:

$$\mathbf{R}^{-1} = \begin{pmatrix} 0 & -\frac{\rho c}{2} & \frac{1}{2} \\ 1 & 0 & -\frac{1}{c^2} \\ 0 & \frac{\rho c}{2} & \frac{1}{2} \end{pmatrix}, \quad (46)$$

where $c = \sqrt{\gamma p / \rho}$ is the speed of sound in the medium. The expressions for \mathbf{R}^{-1} in 3D problems are given in section 7.1 of Wong and Lele [45].

At a midpoint $j + 1/2$, the characteristic variables for all points in the stencil are computed using the same left eigenvector matrix $\mathbf{R}_{j+\frac{1}{2}}^{-1}$ to maintain consistency between the transforms to and back from the characteristic space. $\mathbf{R}_{j+\frac{1}{2}}^{-1}$ is computed using ρ and c values given by the Roe average or arithmetic average of nodes j and $j + 1$. The interpolation scheme for characteristic variables is given by:

$$\begin{aligned} \alpha_{j+\frac{1}{2}}^l \tilde{\xi}_{j-\frac{1}{2}}^l + \beta_{j+\frac{1}{2}}^l \tilde{\xi}_{j+\frac{1}{2}}^l + \gamma_{j+\frac{1}{2}}^l \tilde{\xi}_{j+\frac{3}{2}}^l &= a_{j+\frac{1}{2}}^l \xi_{j-2}^l + b_{j+\frac{1}{2}}^l \xi_{j-1}^l + c_{j+\frac{1}{2}}^l \xi_j^l \\ &+ d_{j+\frac{1}{2}}^l \xi_{j+1}^l + e_{j+\frac{1}{2}}^l \xi_{j+2}^l + f_{j+\frac{1}{2}}^l \xi_{j+3}^l, \quad l = 0, 1, 2, \end{aligned} \quad (47)$$

where $\alpha_{j+\frac{1}{2}}^l$, $\beta_{j+\frac{1}{2}}^l$, $\gamma_{j+\frac{1}{2}}^l$, $a_{j+\frac{1}{2}}^l$, $b_{j+\frac{1}{2}}^l$, $c_{j+\frac{1}{2}}^l$, $d_{j+\frac{1}{2}}^l$, $e_{j+\frac{1}{2}}^l$, and $f_{j+\frac{1}{2}}^l$ are the coefficients obtained from the nonlinear explicit-compact interpolation method described in equation (26). However, the above equation cannot be solved in the form presented above as the interpolated characteristic variables are coupled across grid points due to the compact nature of the interpolation. Solving it in this form would introduce a consistency error since each edge interpolation equation uses a different characteristic matrix for the decomposition. A solution to this is to recast the above equation of scalars to an equation

of vectors of the primitive variables at the cell nodes $\mathbf{V} = (\rho, u, p)^T$ and the unknown midpoint interpolated primitive variables $\tilde{\mathbf{V}} = (\tilde{\rho}, \tilde{u}, \tilde{p})^T$:

$$\begin{aligned} \left(\alpha_{j+\frac{1}{2}} \mathbf{R}_{j+\frac{1}{2}}^{-1}\right) \tilde{\mathbf{V}}_{j-\frac{1}{2}} + \left(\beta_{j+\frac{1}{2}} \mathbf{R}_{j+\frac{1}{2}}^{-1}\right) \tilde{\mathbf{V}}_{j+\frac{1}{2}} + \left(\gamma_{j+\frac{1}{2}} \mathbf{R}_{j+\frac{1}{2}}^{-1}\right) \tilde{\mathbf{V}}_{j+\frac{3}{2}} = \\ \left(a_{j+\frac{1}{2}} \mathbf{R}_{j+\frac{1}{2}}^{-1}\right) \mathbf{V}_{j-2} + \left(b_{j+\frac{1}{2}} \mathbf{R}_{j+\frac{1}{2}}^{-1}\right) \mathbf{V}_{j-1} + \left(c_{j+\frac{1}{2}} \mathbf{R}_{j+\frac{1}{2}}^{-1}\right) \mathbf{V}_j \\ + \left(d_{j+\frac{1}{2}} \mathbf{R}_{j+\frac{1}{2}}^{-1}\right) \mathbf{V}_{j+1} + \left(e_{j+\frac{1}{2}} \mathbf{R}_{j+\frac{1}{2}}^{-1}\right) \mathbf{V}_{j+2} + \left(f_{j+\frac{1}{2}} \mathbf{R}_{j+\frac{1}{2}}^{-1}\right) \mathbf{V}_{j+3}, \end{aligned} \quad (48)$$

where $\alpha_{j+\frac{1}{2}}$, $\beta_{j+\frac{1}{2}}$, $\gamma_{j+\frac{1}{2}}$, $a_{j+\frac{1}{2}}$, $b_{j+\frac{1}{2}}$, $c_{j+\frac{1}{2}}$, $d_{j+\frac{1}{2}}$, $e_{j+\frac{1}{2}}$, and $f_{j+\frac{1}{2}}$ are diagonal matrices with the diagonal entries representing the coefficients obtained using the nonlinear weighting procedure for the corresponding characteristic variable. With the characteristic decomposition, the interpolation reduces to one block tri-diagonal system of equations instead of three tri-diagonal systems of equations if only the primitive variables are interpolated. Note that we only use arithmetic average of node values for the matrix $\mathbf{R}_{j+\frac{1}{2}}^{-1}$ in this work. Section [Appendix C](#) details an efficient algorithm to solve the block-tridiagonal system resulting from this characteristic interpolation.

Figure 10 shows the matrix structure for the left biased characteristic based weighted compact interpolation for the initial conditions of the Shu–Osher problem (section 3.5) with 80 points in the domain. Since the matrix is a block tri-diagonal system, the size of the matrix is 240×240 and the full matrix structure is shown in figure 10(a). Figure 10(b) shows the first 50×50 portion of the interpolation matrix. Here, we see that across the shock at index ~ 24 , the matrix decouples. This means that the interpolation stencil never crosses the shock. Additionally, the point closest to the shock has just one block in its row indicating that the nonlinear weighting procedure picked solely the most upwind stencil at the shock which is purely explicit. Figure 11 shows the left and right interpolated density, velocity, and pressure. Since the interpolation stencil never crosses the shock, the interpolation is virtually perfect and no spurious oscillations are observed.

The method can be easily extended from 1D to multi-dimensional problems by applying the algorithm along each spatial dimension to get the flux derivatives in that direction.

For the 3D Euler equations:

$$\frac{\partial \mathbf{Q}}{\partial t} + \frac{\partial \mathbf{F}(\mathbf{Q})}{\partial x} + \frac{\partial \mathbf{G}(\mathbf{Q})}{\partial y} + \frac{\partial \mathbf{H}(\mathbf{Q})}{\partial z} = 0, \quad (49)$$

the flux derivatives $\partial \mathbf{F}(\mathbf{Q})/\partial x$ are obtained using the algorithm outlined above in the x direction and similarly for the flux derivatives $\partial \mathbf{G}(\mathbf{Q})/\partial y$ and $\partial \mathbf{H}(\mathbf{Q})/\partial z$ in the y and z directions using grid spacings Δy and Δz respectively.

2.7. Cost estimate

The cost estimates for a single left-biased interpolation for the 3D Euler equations using different interpolation schemes are shown in table 3. These are based on the operation count of each sub-algorithm per grid point. The LD nonlinear weights are used for all schemes in this comparison. Although the matrix solve portion of the interpolation algorithm for ECI on characteristic variables is approximately 20 times more expensive

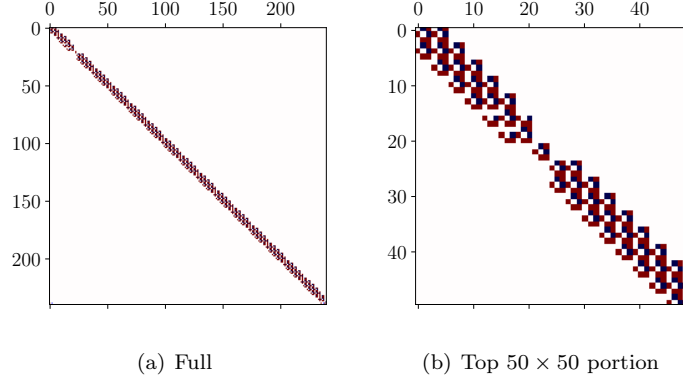


Figure 10: Block tri-diagonal matrix structure for the characteristic decomposition in left-biased interpolation for initial condition of the Shu–Osher problem with 80 points. The top portion of the matrix shows that the interpolation is decoupled across the shock. Red indicates positive values, blue indicates negative values, and white indicates zero values.

than the corresponding EI, this difference is dwarfed by the large operation count of computing the smoothness indicators and nonlinear weights. In total, performing ECI on characteristic variables is $\approx 23\%$ more expensive than performing EI on characteristic variables in terms of the operation count.

Operation counts	Interpolation methods			
	(a)	(b)	(c)	(d)
Matrix solve	0	11	45	195
R.H.S. interpolation	55	55	55	55
Characteristic decomposition	0	66	0	66
Smoothness indicators	440	440	440	440
Nonlinear weights	630	630	720	720
Total	1125	1202	1260	1476

Table 3: Operation counts per grid point for different interpolation methods with the LD nonlinear weights. (a) EI on primitive variables; (b) EI on characteristic variables; (c) ECI on primitive variables; (d) ECI on characteristic variables.

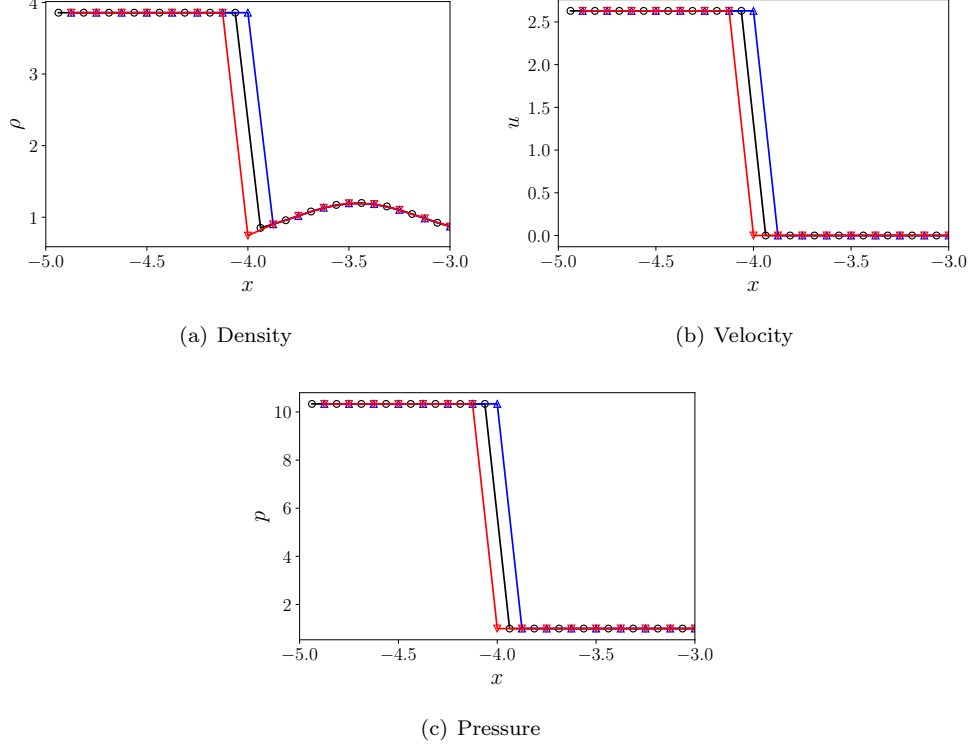


Figure 11: Interpolated values of primitive variables from initial conditions of the Shu–Osher problem with 80 points. Black circles: node values; blue upper triangles: left interpolated midpoint values; red lower triangles: right interpolated midpoint values

2.8. Hybridization of Riemann solvers for multi-dimensional Euler equations

The 3D Euler equations are given by:

$$\frac{\partial \rho}{\partial t} + \nabla \cdot (\rho \mathbf{u}) = 0, \quad (50)$$

$$\frac{\partial \rho \mathbf{u}}{\partial t} + \nabla \cdot (\rho \mathbf{u} \mathbf{u} + p \boldsymbol{\delta}) = 0, \quad (51)$$

$$\frac{\partial E}{\partial t} + \nabla \cdot [(E + p) \mathbf{u}] = 0, \quad (52)$$

where $\mathbf{u} = (u, v, w)^T = (u_1, u_2, u_3)^T$ is the velocity vector.

In this work, we use the hybrid HLLC–HLL Riemann solver proposed by Huang et al. [21] (see [Appendix E](#) for details on the Riemann solver) when the Ducros-like shock sensor [26] value, s , is greater than 0.65. s is defined as:

$$s = \frac{-\theta}{|\theta| + |\boldsymbol{\omega}| + \epsilon}, \quad (53)$$

where $\theta = \nabla \cdot \mathbf{u}$ is the rate of dilatation and $\boldsymbol{\omega} = \nabla \times \mathbf{u}$ is the vorticity. $\epsilon = 1.0\text{e-}15$ is a small constant to prevent division by zero. If $s \leq 0.65$, the HLLC Riemann solver is used instead. The HLLC-HLL Riemann solver is a cure to the HLLC Riemann solver on the potential numerical instabilities near shocks for multi-dimensional problems when the shock normal direction does not align well with the grid normal surface direction.

2.9. Positivity-preserving for Euler equations

Negative density and pressure may arise during the nonlinear interpolation or the numerical time stepping processes to cause numerical failures for WCHR and WCNS's. While first order interpolation can be used instead to ensure that density and pressure are positive when it is detected that the nonlinearly interpolated density or pressure has become negative, a different positivity-preserving approach has to be considered regarding the positivity failures due to time stepping with the finite difference scheme. The positivity-preserving limiter designed by Hu et al. [20] can be a cure for the positivity failures during the time stepping process for Euler problems but requires the use of reconstructed vector flux, $\hat{\mathbf{F}}_{j+\frac{1}{2}}$, from the flux difference form given by equation (39) in the vector form. During time stepping, the positivity-preserving method replaces $\hat{\mathbf{F}}_{j+\frac{1}{2}}$ at any midpoint with a limited flux, $\hat{\mathbf{F}}_{j+\frac{1}{2}}^{**}$, which is given by:

$$\hat{\mathbf{F}}_{j+\frac{1}{2}}^{**} = \left(1 - \theta_{\rho,j+\frac{1}{2}} \theta_{p,j+\frac{1}{2}}\right) \hat{\mathbf{F}}_{j+\frac{1}{2}}^{LF} + \theta_{\rho,j+\frac{1}{2}} \theta_{p,j+\frac{1}{2}} \hat{\mathbf{F}}_{j+\frac{1}{2}}, \quad (54)$$

where $\theta_{\rho,j+\frac{1}{2}}$ and $\theta_{p,j+\frac{1}{2}}$ are blending functions between 0 and 1 to hybridize $\hat{\mathbf{F}}_{j+\frac{1}{2}}$ with the Lax-Friederichs flux, $\hat{\mathbf{F}}_{j+\frac{1}{2}}^{LF}$. $\hat{\mathbf{F}}_{j+\frac{1}{2}}^{LF}$ for 1D Euler equations is given by:

$$\hat{\mathbf{F}}_{j+\frac{1}{2}}^{LF} = \frac{1}{2} [\mathbf{F}_j + \mathbf{F}_{j+1} + (|u| + c)_{\max} (\mathbf{Q}_j - \mathbf{Q}_{j+1})] \quad (55)$$

The procedures to compute $\theta_{\rho,j+\frac{1}{2}}$ and $\theta_{p,j+\frac{1}{2}}$ are given by Hu et al. [20]. The convex combination of the reconstructed flux and the positivity-preserving Lax-Friederichs flux ensures the density and pressure to remain positive for any time stepping method that is a convex combination of Euler-forward time steps under the condition that Courant–Friedrichs–Lewy number, CFL, is smaller than 0.5. In this work, we suggest to use the five-stage fourth order strong stability preserving Runge–Kutta (SSP-RK54) scheme [43] which is a convex combination of Euler-forward steps.

The positivity-preserving flux limiters can be implemented in a dimension-by-dimension fashion for multi-dimensional Euler problems such as 3D problems if the time step size, Δt , is given by the following conditions:

$$\Delta t = \frac{\text{CFL}}{\tau_x + \tau_y + \tau_z}, \quad (56)$$

where

$$\tau_x = \frac{(|u| + c)_{\max}}{\Delta x}, \quad \tau_y = \frac{(|v| + c)_{\max}}{\Delta y}, \quad \tau_z = \frac{(|w| + c)_{\max}}{\Delta z}. \quad (57)$$

2.10. Discretization of viscous and diffusive fluxes for Navier–Stokes equations

The 3D compressible Navier–Stokes equations are given by:

$$\frac{\partial \rho}{\partial t} + \nabla \cdot (\rho \mathbf{u}) = 0, \quad (58)$$

$$\frac{\partial \rho \mathbf{u}}{\partial t} + \nabla \cdot (\rho \mathbf{u} \mathbf{u} + p \boldsymbol{\delta}) - \nabla \cdot \boldsymbol{\tau} = 0, \quad (59)$$

$$\frac{\partial E}{\partial t} + \nabla \cdot [(E + p) \mathbf{u}] - \nabla \cdot (\boldsymbol{\tau} \cdot \mathbf{u} - \mathbf{q}_c) = 0. \quad (60)$$

$\boldsymbol{\tau}$ and \mathbf{q}_c are viscous stress tensor and conductive heat flux respectively. $\boldsymbol{\delta}$ is the identity tensor.

The viscous stress tensor $\boldsymbol{\tau}$ for a Newtonian fluid is given by:

$$\boldsymbol{\tau} = 2\mu \mathbf{S} + \left(\mu_v - \frac{2}{3}\mu \right) \boldsymbol{\delta} (\nabla \cdot \mathbf{u}), \quad (61)$$

where μ and μ_v are the shear viscosity and bulk viscosity respectively. \mathbf{S} is the strain-rate tensor given by:

$$\mathbf{S} = \frac{1}{2} [\nabla \mathbf{u} + (\nabla \mathbf{u})^T]. \quad (62)$$

The conductive flux \mathbf{q}_c is given by:

$$\mathbf{q}_c = -\kappa \nabla T, \quad (63)$$

where κ is the thermal conductivity. T is the temperature given by the equation of state for ideal gas:

$$T = \frac{p}{\rho R}, \quad (64)$$

where R is the gas constant.

All the viscous and diffusive terms are discretized in their non-conservative forms by isolating the Laplacian operator as in Nagarajan et al. [32], Pirozzoli [38]. The viscous term in the momentum equation is split as:

$$\nabla \cdot \boldsymbol{\tau} = \mu (\nabla^2 \mathbf{u} + \nabla \theta) + 2\mathbf{S} \nabla \mu + \lambda \boldsymbol{\delta} \cdot \nabla \theta + \theta \boldsymbol{\delta} \cdot \nabla \lambda, \quad (65)$$

where $\lambda = \mu_v - 2\mu/3$ and $\theta = \nabla \cdot \mathbf{u}$ is the dilatation. The second derivative terms in the gradient of θ are also isolated as:

$$\frac{\partial \theta}{\partial x_i} = \frac{\partial^2 u_i}{\partial x_i^2} + \sum_{k \neq i} \frac{\partial^2 u_k}{\partial x_i \partial x_k}. \quad (66)$$

Summation is not implied by repeating indices in the above equation.

The heat conduction term is split as:

$$\nabla \cdot \mathbf{q}_c = -\kappa \nabla^2 T - \nabla T \cdot \nabla \kappa, \quad (67)$$

and the viscous power term is also split in a non-conservative form as:

$$\nabla \cdot (\boldsymbol{\tau} \cdot \mathbf{u}) = \mathbf{u} \cdot (\nabla \cdot \boldsymbol{\tau}) + \boldsymbol{\tau} : \nabla \mathbf{u}, \quad (68)$$

where equation (65) is used for $\nabla \cdot \boldsymbol{\tau}$.

In equations (65)-(68), the Laplacian and second derivative terms are discretized directly using a sixth order accurate second derivative compact finite difference scheme [28] given by:

$$\frac{2}{15}\hat{f}_{j-1}'' + \frac{11}{15}\hat{f}_j'' + \frac{2}{15}\hat{f}_{j+1}'' = \frac{1}{\Delta x^2} \left[\frac{4}{5}(f_{j+1} - 2f_j + f_{j-1}) + \frac{1}{20}(f_{j+2} - 2f_j + f_{j-2}) \right], \quad (69)$$

where \hat{f}_j'' are numerically approximated second derivatives of any variables f at cell nodes and f_j are f at cell nodes.

The other terms are discretized using successive applications of a sixth order accurate first derivative compact node-to-node finite difference scheme (CND) [28] given by:

$$\frac{1}{5}\hat{f}_{j-1}' + \frac{3}{5}\hat{f}_j' + \frac{1}{5}\hat{f}_{j+1}' = \frac{1}{\Delta x} \left[\frac{7}{15}(f_{j+1} - f_{j-1}) + \frac{1}{60}(f_{j+2} - f_{j-2}) \right], \quad (70)$$

where \hat{f}_j' are numerically approximated first derivatives of any variables f at cell nodes.

3. Numerical results

In this section, we present results using WCNS5-JS, WCNS5-Z, WCNS6-LD, and WCHR6 schemes in different test problems. All tests are inviscid except the compressible homogeneous isotropic turbulence case where the compressible Navier–Stokes equations are used. In all problems, the equations are integrated in time using the five-stage fourth order SSP-RK54 scheme [43]. Positivity-preserving limiter [20] is only used in the 1D planar Sedov blast wave problem and the 2D double Mach reflection problem to overcome the negative density and pressure issues encountered⁴.

3.1. Convergence tests

The formal order of accuracy of each scheme is verified and compared through 1D and 2D problems involving advection of an entropy wave. The initial conditions in a 1D periodic domain $[-1, 1)$ and a 2D periodic domain $[-1, 1) \times [-1, 1)$ are respectively given by:

$$(\rho, u, p) = (1 + 0.5 \sin(\pi x), 1, 1), \quad (71)$$

$$(\rho, u, v, p) = (1 + 0.5 \sin[\pi(x + y)], 1, 1, 1). \quad (72)$$

Since the velocity and pressure are constant and only entropic disturbances are present, the problems reduce to linear advection of the entropy wave. Therefore, the exact solutions are given by:

$$(\rho_{\text{exact}}, u_{\text{exact}}, p_{\text{exact}}) = (1 + 0.5 \sin[\pi(x - t)], 1, 1), \quad (73)$$

$$(\rho_{\text{exact}}, u_{\text{exact}}, v_{\text{exact}}, p_{\text{exact}}) = (1 + 0.5 \sin[\pi(x + y - 2t)], 1, 1, 1). \quad (74)$$

⁴The positivity-preserving limiter has no effect on problems that do not have occurrence of negative density and pressure.

The ratio of specific heats γ is 1.4. The simulations using different schemes are conducted up to $t = 2$ with mesh refinements from $N = 8$ to $N = 128$ points in each direction. All simulations are run with very small constant time steps in order to isolate the spatial error and observe the order of accuracy of different numerical schemes. $\Delta t/\Delta x = 0.02$ is chosen for both 1D and 2D simulations. The L_2 errors for the 1D and 2D problems are computed as:

$$L_2 \text{ error (1D)} = \sqrt{\sum_{j=0}^{N-1} \Delta x (\rho_j - \rho_{\text{exact}}(x_j))^2 / \sum_{j=0}^{N-1} \Delta x}, \quad (75)$$

$$L_2 \text{ error (2D)} = \sqrt{\sum_{i=0}^{N-1} \sum_{j=0}^{N-1} \Delta x \Delta y (\rho_{i,j} - \rho_{\text{exact}}(x_i, y_j))^2 / \sum_{i=0}^{N-1} \sum_{j=0}^{N-1} \Delta x \Delta y}. \quad (76)$$

From tables 4 and 5 together with figure 12, we can see that all schemes can achieve their formal orders of accuracy when the number of points is large enough. Although both WCNS6-LD and WCHR6 are sixth order accurate, the latter scheme is more accurate than the former with errors that are $\approx 4 - 5$ times smaller. This is consistent with the ratio of their respective interpolation truncation errors which is $34/7 \approx 4.86$ since the major difference between the two schemes is the interpolation method.

Number of points	WCNS5-JS		WCNS5-Z		WCNS6-LD		WCHR6	
	error	order	error	order	error	order	error	order
8	2.993e-02		8.328e-03		2.410e-03		6.339e-04	
16	1.954e-03	3.94	2.453e-04	5.09	4.028e-05	5.90	9.663e-06	6.04
32	6.321e-05	4.95	7.579e-06	5.02	6.399e-07	5.98	1.500e-07	6.01
64	1.905e-06	5.05	2.372e-07	5.00	1.004e-08	5.99	2.339e-09	6.00
128	5.817e-08	5.03	7.416e-09	5.00	1.570e-10	6.00	3.697e-11	5.98

Table 4: L_2 errors and orders of convergence of density for the 1D problem from different schemes at $t = 2$.

Number of points	WCNS5-JS		WCNS5-Z		WCNS6-LD		WCHR6	
	error	order	error	order	error	order	error	order
8^2	5.712e-02		1.647e-02		4.807e-03		1.265e-03	
16^2	3.519e-03	4.02	4.915e-04	5.07	8.046e-05	5.90	1.930e-05	6.03
32^2	1.235e-04	4.83	1.526e-05	5.01	1.279e-06	5.98	2.999e-07	6.01
64^2	3.793e-06	5.02	4.778e-07	5.00	2.008e-08	5.99	4.683e-09	6.00
128^2	1.165e-07	5.03	1.494e-08	5.00	3.140e-10	6.00	7.332e-11	6.00

Table 5: L_2 errors and orders of convergence of density for the 2D problem from different schemes at $t = 2$.

3.2. Advection of broadband disturbances

This problem is similar to the earlier one but with the density field of a uniform flow being disturbed by a broadband signal instead of a single mode. The initial conditions

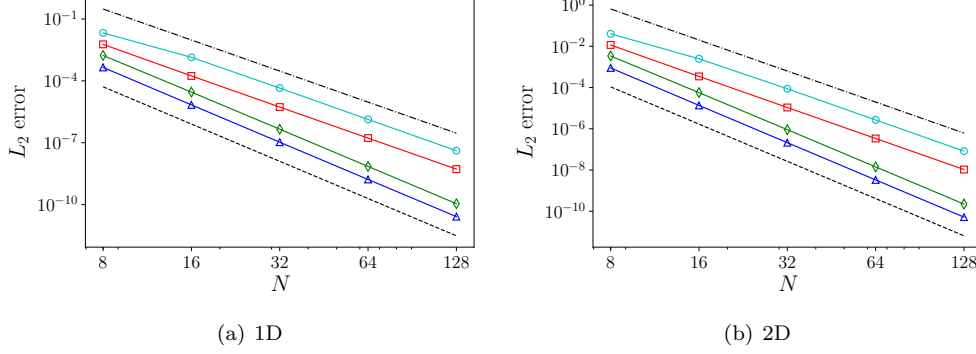


Figure 12: L_2 errors against numbers of points, N , of different schemes for the 1D and 2D convergence tests. Cyan circles: WCNS5-JS; red squares: WCNS5-Z; green diamonds: WCNS6-LD; blue triangles: WCHR6; dashed-dotted line: fifth-order; dashed line: sixth-order

are given by:

$$\begin{pmatrix} \rho \\ u \\ p \end{pmatrix} = \begin{pmatrix} 1 + \delta \sum_{k=1}^{N/2} (E_\rho(k))^{1/2} \sin(2\pi k(x + \psi_k)) \\ 1 \\ 1 \end{pmatrix}, \quad (77)$$

where ψ_k is a random number between 0 and 1 with uniform distribution, $\delta = 1.0\text{e-}2$, and the ratio of specific heats γ is 1.4. The density spectrum $E_\rho(k)$ is given by:

$$E_\rho(k) = \left(\frac{k}{k_0}\right)^4 \exp\left(-2\left(\frac{k}{k_0}\right)^2\right). \quad (78)$$

We have chosen $k_0 = 12$. The computational domain is periodic on domain $x \in [0, 1]$. The simulations are run with $N = 128$ and $\Delta t = 0.002$ until $t = 1$.

The density solutions from various schemes after one period are shown in figure 13(a). Since this problem reduces to linear advection, we should expect the initial density spectrum to be preserved without any corruption. However, the schemes themselves are nonlinear and would introduce some coupling between different modes. Figure 13(b) compares the spectra of the density disturbance from different schemes. We see that both WCNS5-JS and WCNS5-Z are too dissipative to preserve the initial spectrum due to their upwind nature. WCNS6-LD preserves the initial spectrum better, but still has some deviations from the prescribed spectrum. WCHR6 preserves the initial spectrum virtually perfectly. Unlike the WCNS's almost no errors due to the nonlinear nature of the scheme are seen. This is attributed to its higher resolution characteristics.

3.3. Entropy wave leaving domain

In this 1D inviscid problem, the advection of a Gaussian entropy wave leaving a domain $x \in [0, 1]$ is simulated with the WCHR scheme and boundary closures. The initial conditions are given by:

$$(\rho, u, p) = \left(1 + 0.1 \exp\left(-400(x - 0.5)^2\right), 0.5, 1\right). \quad (79)$$

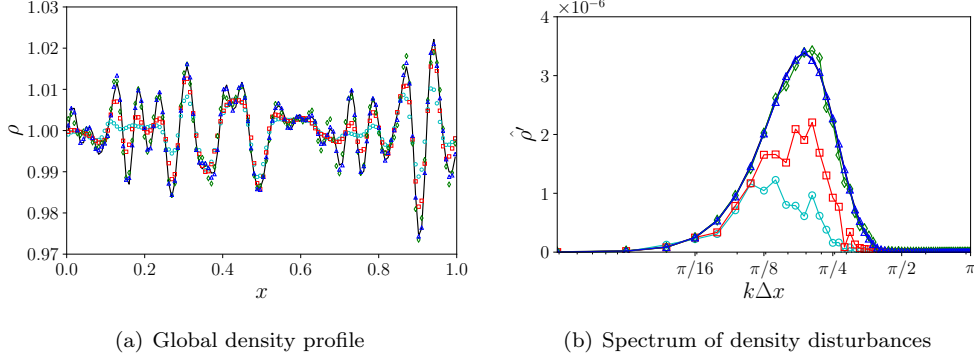


Figure 13: Advection of broadband disturbances problem at $t = 1.0$ using different schemes. Black solid line: exact; cyan circles: WCNS5-JS; red squares: WCNS5-Z; green diamonds: WCNS6-LD; blue triangles: WCHR6.

The ratio of specific heats γ is 1.4. As the Gaussian pulse is being advected, it eventually reaches the right boundary and leaves the domain. Two boundary treatment methods to fill ghost cells at the boundaries are compared: (1) constant extrapolation from interior solutions and (2) sub-sonic inflow and outflow boundary conditions at the left and right boundaries respectively following the non-reflective characteristic ghost cell method in Motheau et al. [31].

Primitive variables are used for the constant extrapolation method. For the non-reflective subsonic outflow method, $\sigma = 0.005$, $l_x = 0.1$, and $p_t = 1$ are used. As for the non-reflective subsonic inflow method, $\eta_2 = \eta_3 = 0.005$, $l_x = 0.1$, $u_t = 0.5$, and $(p/\rho)_t = RT_t = 1$ are set. The details of the implementation of the non-reflective characteristic method as well as interpretation of the parameters detailed above are explained in [31]. Simulations are performed with constant time steps $\Delta t = 0.002$ on a uniform grid composed of $N = 128$ grid points.

From figures 14 and 15, it can be seen that both boundary methods allow the entropy wave to leave the domain when they are used with the boundary schemes in section 2.5. Figure 16 shows that the L_∞ errors of pressure are very small for both methods. This indicates that acoustic components of any unphysical reflections at the outflow boundary are insignificant for both methods. However, the non-reflective characteristic method outperforms the extrapolation method in accuracy of the solution of density field at different times which shows the necessity of non-reflective characteristic method in the boundary treatment to properly treat the outgoing entropic wave.

3.4. Sod shock tube problem

This is a 1D shock tube problem introduced by Sod [42]. The problem consists of the propagation of a shock wave, a contact discontinuity, and an expansion fan. The initial conditions are given by:

$$(\rho, u, p) = \begin{cases} (1, 0, 1), & x < 0, \\ (0.125, 0, 0.1), & x \geq 0. \end{cases} \quad (80)$$

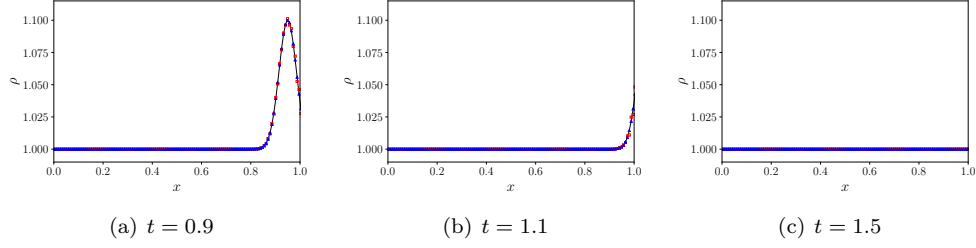


Figure 14: Global density profiles for the entropy wave leaving domain problem at different times. Black solid line: exact; red squares: extrapolation; blue triangles: non-reflective characteristic boundary conditions.

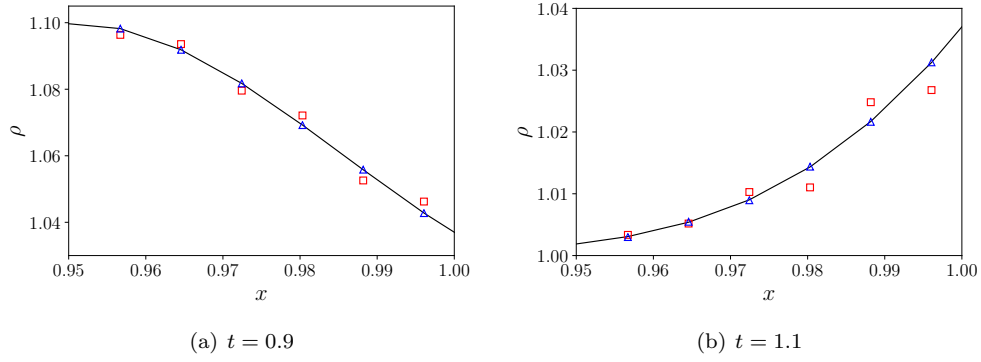


Figure 15: Local density profiles for the entropy wave leaving domain problem at different times. Black solid line: exact; red squares: extrapolation; blue triangles: non-reflective characteristic boundary conditions.

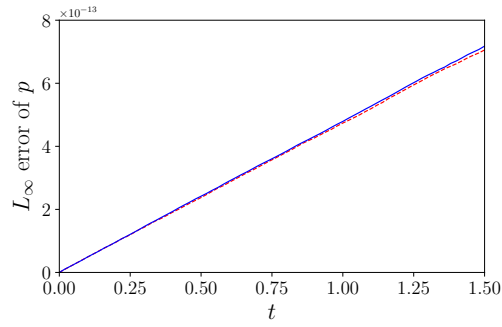


Figure 16: L_∞ errors of pressure against time for the entropy wave leaving domain problem. Red dashed line: extrapolation; blue solid line: non-reflective characteristic boundary conditions.

The ratio of specific heats γ is 1.4. The computational domain has size $x \in [-0.5, 0.5]$. Simulations are performed with constant time steps $\Delta t = 0.002$ on a uniform grid composed of 100 grid points where $\Delta x = 0.01$.

Comparison between the exact solution and the numerical solution for the density at $t = 0.2$ is shown in figure 17. It can be seen that all of the schemes can capture the shock well. WCHR6 and WCNS6-LD have sharper profiles at the shock in comparison to WCNS5-JS and WCNS5-Z.

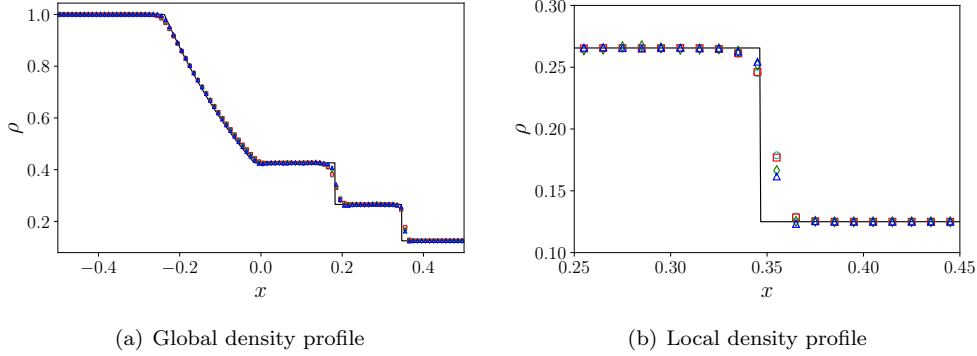


Figure 17: Sod shock tube problem at $t = 0.2$ using different schemes. Black solid line: exact; cyan circles: WCNS5-JS; red squares: WCNS5-Z; green diamonds: WCNS6-LD; blue triangles: WCHR6.

3.5. Shu–Osher problem

This 1D problem first proposed by Shu and Osher [41] involves the interaction of a Mach 3 shock wave with an entropy wave. The interaction creates a high wavenumber entropy wave and a nonlinear acoustic wave that steepens and forms a shock train. This problem can hence assess the ability of a scheme to capture discontinuities well, while also retaining the smooth features of the solution. The initial conditions are given by:

$$(\rho, u, p) = \begin{cases} (27/7, 4\sqrt{35}/9, 31/3), & x < -4, \\ (1 + 0.2 \sin(5x), 0, 1), & x \geq -4. \end{cases} \quad (81)$$

The ratio of specific heats γ is 1.4. The spatial domain of the problem is $x \in [-5, 5]$. Simulations are conducted with constant time steps $\Delta t = 0.005$ on a uniform grid with 150 grid points and also with constant time steps $\Delta t = 0.004$ on a uniform grid with 200 grid points. A reference solution is computed using the WCNS6-LD scheme with 2000 points and time step of $\Delta t = 0.0002$. All results shown here are at time $t = 1.8$.

Figures 18 and 19 show the density profile at $t = 1.8$ obtained using various schemes compared to the reference solution with the two different grid resolutions. Both WCNS5-JS and WCNS5-Z dissipate the high wavenumber entropy wave significantly which is not seen in the results from the WCNS6-LD and WCHR6 schemes. Figure 18(b) shows that WCHR6 has less dispersion error around the region where the entropy wave and weak shock interacts from the results with 150 points due to the higher resolution characteristics of WCHR6.

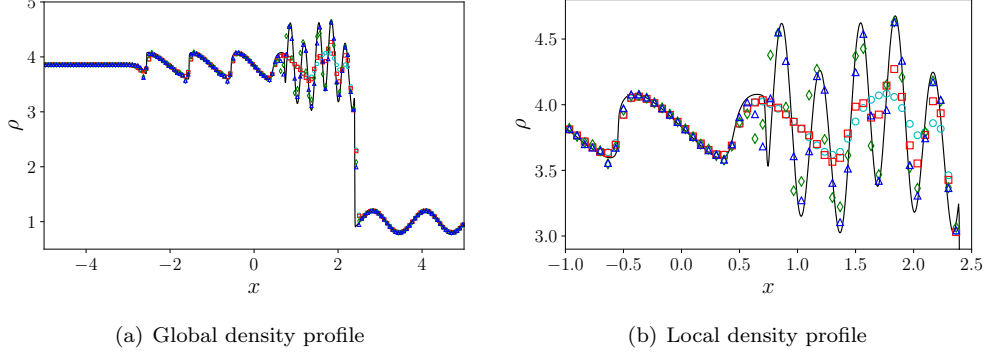


Figure 18: Shu–Osher problem at $t = 0.2$ using different schemes with $\Delta x = 1/15$. Black solid line: reference; cyan circles: WCNS5-JS; red squares: WCNS5-Z; green diamonds: WCNS6-LD; blue triangles: WCHR6.

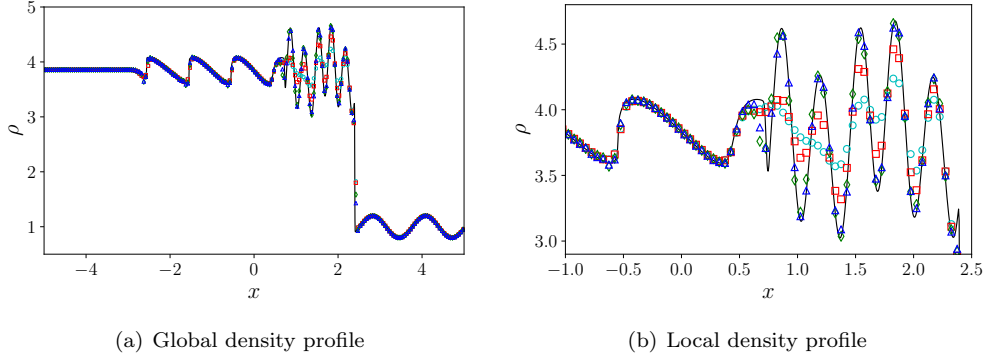


Figure 19: Shu–Osher problem at $t = 0.2$ using different schemes with $\Delta x = 0.05$. Black solid line: reference; cyan circles: WCNS5-JS; red squares: WCNS5-Z; green diamonds: WCNS6-LD; blue triangles: WCHR6.

3.6. One-dimensional planar Sedov blast wave problem

This 1D planar Sedov blast wave problem [39, 49, 20] is a near vacuum problem with the propagation of blast waves. The initial conditions are given by:

$$(\rho, u, p) = \begin{cases} (1, 0, 4.0\text{e-}13), & x < 2 - 0.5\Delta x, \ x > 2 + 0.5\Delta x, \\ (1, 0, \frac{1.28\text{e6}}{\Delta x}), & 2 - 0.5\Delta x \leq x \leq 2 + 0.5\Delta x. \end{cases} \quad (82)$$

The ratio of specific heats γ is 1.4. The spatial domain of the problem is $x \in [0, 4]$. Simulations are conducted with constant time steps $\Delta t = 1.0\text{e-}6$ on a uniform grid with 201 grid points.

Figures 20(a) and 20(b) show the density and pressure profiles respectively at $t = 1.0\text{e-}3$ obtained using various schemes with the positivity limiter. It can be seen that

all of the schemes can capture the blast waves. However, the pressure profiles computed with WCHR6 and WCNS6-LD have small overshoots at the peaks of the blast waves while density and pressure peaks obtained with WCNS5-JS and WCNS5-Z are damped.

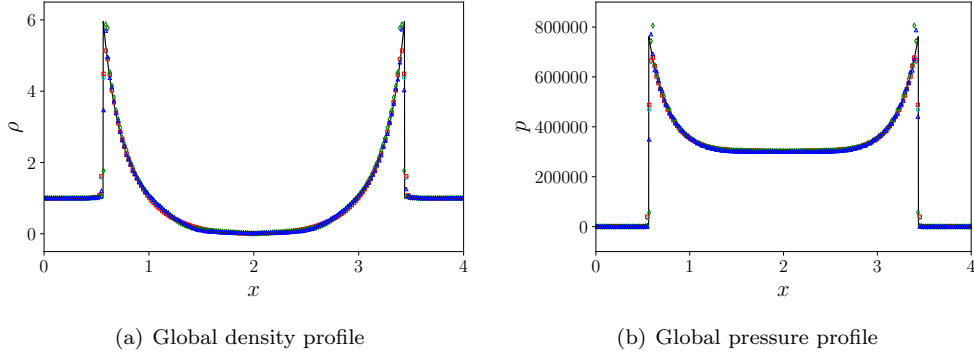


Figure 20: 1D planar Sedov blast wave problem at $t = 1.0\text{e-}3$ using different schemes. Black solid line: exact; cyan circles: WCNS5-JS; red squares: WCNS5-Z; green diamonds: WCNS6-LD; blue triangles: WCHR6.

3.7. Two-dimensional vortex leaving domain

This is a 2D test problem of the advection of an isothermal vortex out of a computation domain in a Mach number $M_\infty = 0.283$ uniform flow following case C in Granet et al. [15] except that inviscid conditions are used here. The initial conditions of the vortex⁵ are given by:

$$\begin{pmatrix} \rho \\ p \\ \delta u \\ \delta v \end{pmatrix} = \begin{pmatrix} \rho_\infty \exp \left[-\frac{\gamma}{2} \left(\frac{\Gamma_v}{c R_v} \right)^2 \exp \left(-\left(\frac{r}{R_v} \right)^2 \right) \right] \\ p_\infty \exp \left[-\frac{\gamma}{2} \left(\frac{\Gamma_v}{c R_v} \right)^2 \exp \left(-\left(\frac{r}{R_v} \right)^2 \right) \right] \\ -\frac{\Gamma_v}{R_v^2} \exp \left[-\frac{1}{2} \left(\frac{r}{R_v} \right)^2 \right] (y - y_v) \\ \frac{\Gamma_v}{R_v^2} \exp \left[-\frac{1}{2} \left(\frac{r}{R_v} \right)^2 \right] (x - x_v) \end{pmatrix}, \quad (83)$$

where $\Gamma_v = 0.024$, $R_v = 0.1$. The background flow has $\rho_\infty = 1$, $p_\infty = 1/\gamma$, $u_\infty = M_\infty c_\infty$, $v_\infty = 0$, and $c_\infty = 1$. δu and δv are the deviations of the u and v velocities from u_∞ and v_∞ respectively. The ratio of specific heats $\gamma = 1.4$ is used. The problem domain is chosen to be $[-D/2, D/2] \times [-D/2, D/2]$, where $D = 1$ and the problem is periodic in the y direction. The vortex is located at $(x_v, y_v) = (0, 0)$ initially. Figure 21 shows the initial configuration and computation domain.

⁵This is actually a swirling flow with zero net circulation in the far field.

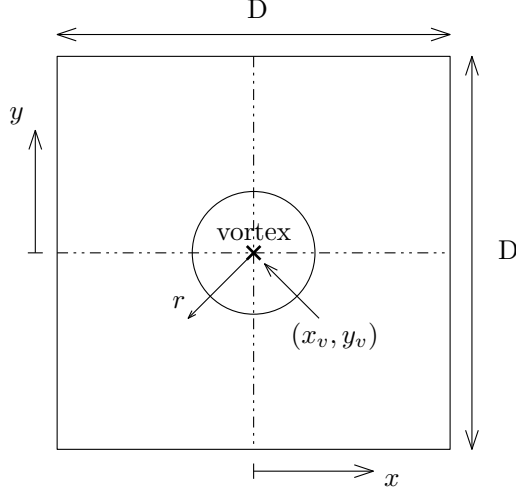


Figure 21: Schematic diagram of initial flow field and computational domain of the vortex leaving domain problem.

Similar to the 1D entropy wave leaving domain problem, the boundary schemes with two different ghost cell filling methods: (1) constant extrapolation of primitive variables from interior solutions and (2) sub-sonic inflow and outflow non-reflective boundary conditions at the left and right boundaries following Motheau et al. [31] are tested in this problem. When the non-reflective methods are used, $\sigma = 0.005$, $l_x = R_v$, $\beta = M_\infty$, and $p_t = p_\infty$ are used for the non-reflective subsonic outflow method and $\eta_2 = \eta_3 = \eta_4 = 0.005$, $l_x = R_v$, $\beta = M_\infty$, $u_t = u_\infty$, and $(p/\rho)_t = RT_t = p_\infty/\rho_\infty$ are set for the non-reflective subsonic inflow method. All simulations in this section are run with CFL = 0.5 and a grid with 64×64 points is used.

Simulations computed with the boundary schemes and both ghost cell methods give stable results. Figure 22 shows the streamwise velocity contours and the normalized pressure field at different normalized times computed with the two different boundary treatments. The pressure field and time are normalized as:

$$p^* = (p_\infty - p) \frac{2R_v^2}{\rho_\infty \Gamma_v^2}, \quad (84)$$

$$t^* = \frac{2u_\infty t}{D}. \quad (85)$$

From the figures, it can be seen that the non-reflective boundary condition methods give accurate results, without any spurious waves reflected at the boundaries. However, in the solutions computed with the extrapolation method, spurious pressure waves are introduced at the right outflow boundary and the vortex is highly distorted as it crosses the domain boundary. These findings are similar to those observed in Motheau et al. [31].

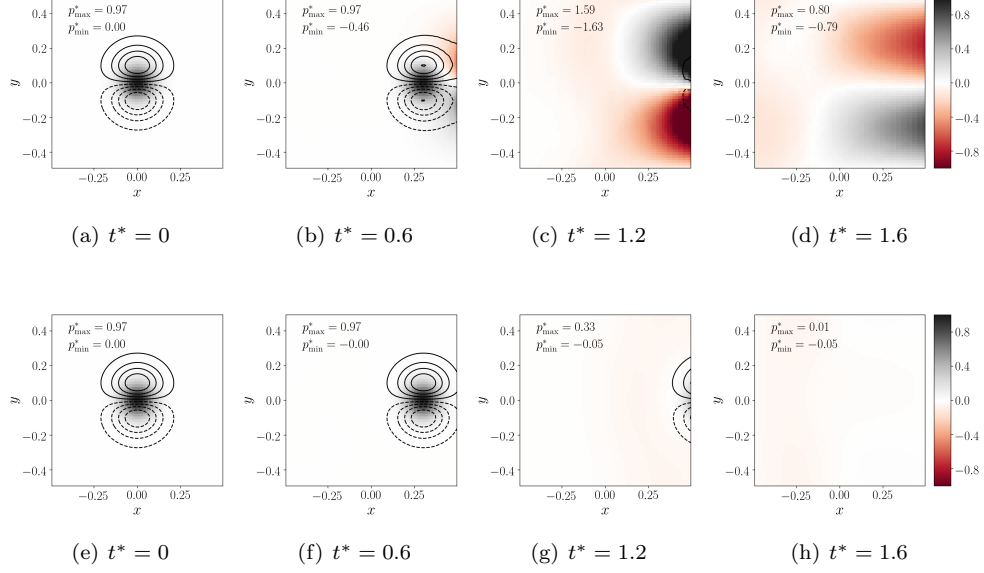


Figure 22: 10 equally spaced streamwise velocity contours from 0.137 to 0.429 and normalized pressure fields, p^* , for the vortex leaving domain problem at different normalized times computed with the extrapolation boundary treatment (top row) and the non-reflecting boundary treatment (bottom row).

3.8. Two-dimensional shock-vortex interaction

This 2D shock-vortex interaction problem was studied previously in several papers [22, 47, 5]. The inviscid version of this problem is studied here which consists of a stationary Mach 1.2 shock and a strong isentropic vortex⁶ characterized by the vortex Mach number M_v initially in the pre-shock region. The initial configuration and computation domain are shown in figure 23. The shock is at $x = 0$ and the vortex is located upstream of the shock at $(x_v, y_v) = (D/10, 0)$ initially. The initial conditions of the vortex are given by:

$$\begin{pmatrix} \rho \\ p \\ \delta u \\ \delta v \end{pmatrix} = \begin{pmatrix} \rho_\infty \left[1 - \frac{1}{2} (\gamma - 1) M_v^2 \exp \left(1 - \left(\frac{r}{R_v} \right)^2 \right) \right]^{\frac{1}{\gamma-1}} \\ p_\infty \left[1 - \frac{1}{2} (\gamma - 1) M_v^2 \exp \left(1 - \left(\frac{r}{R_v} \right)^2 \right) \right]^{\frac{\gamma}{\gamma-1}} \\ - \frac{M_v c_\infty}{R_v} \exp \left[\frac{1}{2} \left(1 - \left(\frac{r}{R_v} \right)^2 \right) \right] (y - y_v) \\ \frac{M_v c_\infty}{R_v} \exp \left[\frac{1}{2} \left(1 - \left(\frac{r}{R_v} \right)^2 \right) \right] (x - x_v) \end{pmatrix}. \quad (86)$$

where $\rho_\infty = 1.0$, $p_\infty = 1/\gamma$, $u_\infty = M_\infty c_\infty$, $v_\infty = 0$, $c_\infty = 1$, $M_v = 1.0$, and vortex radius $R_v = 1.0$ are chosen in this paper. δu and δv are the deviations of the u and v velocities

⁶Like in the previous problem, this is also actually a swirling flow with zero net circulation in the far field.

from u_∞ and v_∞ respectively. The ratio of specific heats $\gamma = 1.4$ is used. The problem domain is chosen to be $[-3D/4, D/4] \times [-D/2, D/2]$, where $D = 40$ and the problem is periodic in the y direction. The shock is initialized at $x = 0$. Dirichlet post-shock and pre-shock boundary conditions are used to fill ghost cells for the boundary schemes at the left and right boundaries. A 2D grid with 512×512 points is used for all the schemes. All cases in this section are run with $\text{CFL} = 0.5$.

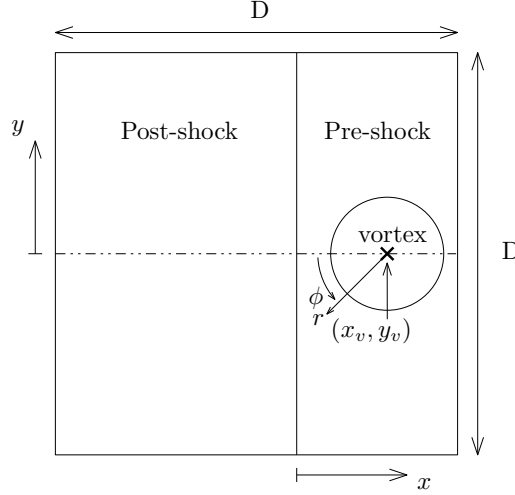


Figure 23: Schematic diagram of initial flow field and computational domain of the shock-vortex interaction problem.

Figure 24 shows the pressure fields at $t = 6$ for the four different schemes. At this time instant, the vortex has passed through the nominal shock line, but its interaction with the shock leads to several curved and highly deformed shock structures. WCNS5-JS and WCNS5-Z are dissipative but yield non-oscillatory solutions. WCNS6-LD and WCHR6 are less dissipative and have crispier features. However, they both have some mild oscillations at the radial shock front.

Figure 25 shows the sound pressure fields defined as $(p - p_\infty) / (\rho_\infty c_\infty^2)$ at $t = 16$ for the four different schemes. Here, the $(\cdot)_\infty$ quantities are all taken to be the post-shock values. The vortex, having passed through the shock gets deformed and as a result we see a quadrupole sound signature. However, since the vortex strength is very high, many weak shock waves are generated and propagate radially outward. Again, from figure 25, we see that WCNS5-JS and WCNS5-Z are more dissipative and damp the fine-scale structures of the sound field. WCNS6-LD and WCHR6 are less dissipative and have more fine-scale features. Figure 26 shows the sound pressure on a radial line from the center of the vortex with an angle of $\phi = -45^\circ$ (see figure 23) for the four schemes considered here and a reference solution obtained using the WCNS5-Z on a grid with eight times the number of points in each direction. Figure 26(a) plots a global view of the radial sound pressure profile and all schemes seem to overlap with the reference solution at this scale. Figure 26(b) shows a local view of the outgoing shock front at $r \approx 14.5$. Here we see that WCHR6 and WCNS6-LD overshoot the peak sound pressure while the WCNS5-JS and WCNS5-Z under-predict the peak sound pressure level. Figure 26(c)

shows a local view of the radial sound pressure profile around $r = 7.5$. Here, the local peak of the sound pressure profile in the reference solution is not captured by any of the WCNS's while the WCHR6 scheme is able to capture the peak owing to its higher resolution property.

3.9. Double Mach reflection

This is a 2D problem with the domain size of $[0, 4] \times [0, 1]$ by Woodward and Colella [46]. The initial conditions are given by:

$$(\rho, u, v, p) = \begin{cases} (8, 8.25 \cos(\frac{\pi}{6}), -8.25 \sin(\frac{\pi}{6}), 116.5), & x < \frac{1}{6} + \frac{y}{\sqrt{3}}, \\ (1.4, 0, 0, 1), & x \geq \frac{1}{6} + \frac{y}{\sqrt{3}}. \end{cases}$$

A Mach 10 strong shock initially makes a 60° angle with the horizontal wall at location $x = 1/6$ of the bottom boundary. As the shock moves and reflects on the wall, a complex shock structure with two triple points appears. The ratio of specific heats is $\gamma = 1.4$. The boundary conditions following those by Woodward and Colella [46] are used. At the bottom boundary, the conditions in the region $x \in [0, 1/6]$ are fixed at Dirichlet boundary conditions with the post-shock flow conditions and reflecting boundary conditions are used for $x \geq 1/6$. Dirichlet boundary conditions with the post-shock flow conditions are set at the left boundary. Constant extrapolations of primitive variables are used to fill ghost cells at the right boundary to allow zero-gradient boundary conditions. Time-dependent conditions are applied on the top boundary to match the movement of the shock wave. The simulations are conducted with constant CFL = 0.5 until $t = 0.2$. All schemes can only provide stable results with the positivity limiter. The density fields for different schemes at $t = 0.2$ are shown in figure 28.

At the shock triple point, a slip line is generated that is Kelvin–Helmholtz unstable. Since the inviscid Euler equations are solved, there is no physical dissipation in this test problem. The instability of the vortex sheet along the slip line is only damped by numerical dissipation. From figure 28, we see that with the same mesh resolution of 960×240 , both WCNS5-JS and WCNS5-Z are numerically too dissipative and completely inhibit the growth of Kelvin–Helmholtz vortices along the slip lines. On the other hand, both WCNS6-LD and WCHR6 can capture much more small-scale vortical structures along the slip lines as more localized dissipation is applied at the discontinuities. Since WCHR6 is the least dissipative, it exhibits the highest level of instability growth.

3.10. Taylor–Green vortex

The 3D inviscid Taylor–Green vortex problem is a popular test case used to compare the numerical dissipation of different schemes and has been used widely in previous literature [24, 18]. The initial conditions of the problem are given by:

$$\begin{pmatrix} \rho \\ u \\ v \\ w \\ p \end{pmatrix} = \begin{pmatrix} 1 \\ \sin x \cos y \cos z \\ -\cos x \sin y \cos z \\ 0 \\ 100 + \frac{(\cos(2z)+2)(\cos(2x)+\cos(2y))-2}{16} \end{pmatrix}. \quad (87)$$

The ratio of specific heats of the gas is $\gamma = 5/3$. The domain is periodic with size $[0, 2\pi)^3$. The problem is solved with the four schemes considered here on a 64^3 grid. Simulations are conducted until $t = 10$ with a constant CFL = 0.6.

As the mean pressure is chosen to be very large compared to the dynamic pressure, the flow problem is essentially incompressible. Thus, the kinetic energy of the flow is conserved in the inviscid limit and the problem can be used as a test to examine the dissipative property of different schemes. As time evolves, the initial flow gets stretched and energy is transferred from larger to finer scales.

Figure 29 plots the kinetic energy ($\langle \rho u_i u_i \rangle / 2$) and enstrophy ($\langle \omega_i \omega_i \rangle$) normalized by their respective initial values. The $\langle \cdot \rangle$ operator indicates averaging in space. Here, we see that WCHR6 is the least dissipative and retains the largest amount of the kinetic energy at $t = 10$. Both upwind biased schemes (WCNS5-JS and WCNS5-Z) are more dissipative than the hybrid central-upwind schemes (WCHR6 and WCNS6-LD). Similar trends can also be seen in the enstrophy plot. WCHR6 captures significantly larger amount of enstrophy compared to WCNS6-LD while the upwind biased schemes are very dissipative and deviate from the semi-analytical solution of Brachet et al. [4] much earlier than the hybrid central-upwind schemes.

Figures 30 and 31 compare the velocity and vorticity spectra of various schemes at $t = 5$ and $t = 7$ respectively. These spectra are also compared to a higher resolution simulation with 256^3 grid points performed using a tenth order compact finite difference scheme [28] with localized artificial dissipation. The velocity spectra are much more revealing than the kinetic energy plot. WCHR6 is the least dissipative since it is able to preserve more high wavenumber features while the other schemes dissipate the high wavenumber content more aggressively. WCHR6 agrees well with the higher resolution case until the Nyquist limit ($k = 32$) at $t = 5$ while WCNS6-LD agrees well till $k \approx 17$ after which it starts becoming more dissipative. WCNS5-JS and WCNS5-Z start adding dissipation from $k \approx 5$. The vorticity spectrum highlights the high wavenumber content more. From the vorticity spectrum, we again see that WCHR6 has much more energy in the high wavenumber region compared to the WCNS's. At $t = 7$, the flow has much more fine scale features. At this time, all the schemes deviate from the high resolution case. The WCHR6 scheme has the highest energy content among all the other schemes and is closest to the high resolution case at all wavenumbers.

3.11. Compressible homogeneous isotropic turbulence

A more realistic and pertinent test case for shock-capturing schemes than the Taylor–Green vortex problem is the decay of compressible homogeneous isotropic turbulence [27, 24]. This is a viscous test case with the initial RMS velocity fluctuations being large enough to create eddy shocklets [27] and serves as a good problem to test the ability of numerical methods to capture shocks while also examine their dissipation characteristics for turbulence.

The initial velocity profile is a random solenoidal field that has an energy spectrum given by:

$$E(k) \propto k^4 \exp \left(-2 \left(\frac{k}{k_0} \right)^2 \right), \quad (88)$$

where k is the wavenumber and k_0 is the most energetic wavenumber. This gives an initial Taylor microscale, $\lambda = \lambda_0 = 2/k_0$. The RMS velocity fluctuation is given by

$u_{\text{rms}} = \sqrt{\langle u_i u_i \rangle / 3} = \sqrt{(2/3) \int_0^\infty E(k) dk}$. Details in obtaining the initial velocity profiles can be found in Johnsen et al. [24]

The two important parameters in this problem are the turbulent Mach number, $M_t = \sqrt{3} u_{\text{rms}} / \langle c \rangle$, and the Taylor scale Reynolds number, $\text{Re}_\lambda = \langle \rho \rangle u_{\text{rms}} \lambda / \langle \mu \rangle$. In this section, we consider the case with $M_t = M_{t,0} = 0.6$, $\text{Re}_\lambda = \text{Re}_{\lambda,0} = 100$, and $k_0 = 4$ initially. Ratio of specific heats, $\gamma = 1.4$, and the gas constant, $R = 1$, are used. The density and pressure fields are taken to be constant at $\rho = 1$ and $p = 1/\gamma$ initially.

The shear viscosity is assumed to follow a power law temperature dependence given by:

$$\frac{\mu}{\mu_{\text{ref}}} = \left(\frac{T}{T_{\text{ref}}} \right)^{\frac{3}{4}}, \quad (89)$$

where $T_{\text{ref}} = 1/\gamma$ and $\mu_{\text{ref}} = u_{\text{rms},0} \lambda_0 / \text{Re}_{\lambda,0}$. $u_{\text{rms},0}$ is the initial u_{rms} . The bulk viscosity, μ_v , is assumed to be zero. A constant Prandtl number, $\text{Pr} = 0.7$, is used. The Prandtl number is defined as:

$$\text{Pr} = \frac{c_p \mu}{\kappa}, \quad c_p = \frac{\gamma R}{\gamma - 1} \quad (90)$$

The domain is periodic with size $[0, 2\pi]^3$. The problem is solved on a 64^3 grid with the four schemes considered in this work. Reference solutions obtained from a direct numerical simulation (DNS) dataset spectrally filtered to a 64^3 grid are used for comparison. The DNS dataset is obtained using a 512^3 grid and a tenth order compact finite difference scheme. See section [Appendix F](#) for details on how the spectrally filtered DNS solutions are obtained. Simulations are run with a constant $\text{CFL} = 0.5$ until $t/\tau = 4$ where τ is the eddy turnover time given by $\tau = \lambda_0 / u_{\text{rms},0}$. The simulations are also performed without the use of a subgrid-scale model in order to test the dissipation characteristics of the numerical scheme alone. Addition of subgrid-scale models in conjunction with this shock capturing scheme in a suitable and consistent way is left for future work.

Figure [32\(a\)](#) shows the numerical schlieren visualizing eddy shocklets in the domain. Figure [32\(b\)](#) shows contours of high enstrophy and high negative dilatation that visualizes the eddy shocklets. These distributed eddy shocklets make this test case challenging for numerical schemes and highlights the ability of schemes to capture turbulence structures as well as discontinuities. Figure [33](#) shows the velocity variance, enstrophy, and dilatation variance as a function of time for the four schemes and the filtered DNS solution. Here, we see that WCHR6 is the least dissipative and is the closest to the filtered DNS profiles for all the three statistics plotted. The enstrophy profiles highlight the difference between the schemes. WCNS5-JS and WCNS5-Z are excessively dissipative and capture very little amount of the enstrophy. WCHR6 agrees the best with the filtered DNS solution and shows that it is minimally dissipative even in the presence of eddy shocklets. Similar trends are seen in the plot of the dilatation variance. WCHR6 agrees very well with the filtered DNS solution while the other schemes dissipate dilatational motions more.

Figures [34](#) and [35](#) show the velocity, vorticity, dilatation, and density spectra for the four different schemes. At this $\text{Re}_{\lambda,0}$ of 100, the peak of the vorticity energy spectrum is at $k \approx 9$ which is well below the maximum resolvable wavenumber of 32. The two fifth order schemes don't capture this peak well but the two sixth order schemes do. Similar to the Taylor–Green vortex case, it can be seen that WCHR6 is the best at capturing fine scale features in both vorticity and dilatation while this advantage is less pronounced in this lower Reynolds number test case.

4. Conclusions

In summary, we have developed a new sixth order accurate weighted compact high resolution (WCHR6) scheme that has higher resolution and more localized dissipation than previous WCNS's. The high resolution property primarily comes from incorporating compact interpolation schemes directly into the WCNS interpolation mechanism. The scheme is presented for use with conservation equations such as the Euler equations and compressible Navier–Stokes equations in one, two, and three dimensions. The block tri-diagonal characteristic decomposition method is shown to be effective at interpolating primitive variables across shocks. Approximate dispersion relation (ADR) analysis of the scheme shows the superior resolution ability of the scheme compared to other WCNS's of similar orders of accuracy that use only explicit interpolations. Appropriate boundary schemes are also developed for non-periodic problems. Further, a conservative flux-difference form of compact finite difference schemes was derived for the first time and this allowed the use of central compact finite difference schemes with positivity-preserving limiters. Sixth order of accuracy of the scheme was demonstrated for the advection of an entropy wave in 1D and multi-dimensional settings. For all the test problems, the WCHR6 scheme was compared with WCNS's that utilized the same compact finite difference scheme but different interpolation methods to highlight the benefit of the new compact nonlinear interpolation method. Since all WCNS's in this paper use the same compact finite difference scheme as WCHR6, the advantage of the WCHR6 scheme might be expected to be larger when compared to the versions of the WCNS's which use explicit finite difference schemes. The advection of a broadband entropy wave showed that the WCHR6 scheme was better than the WCNS's at preserving the spectral content of the solution. The 1D Sod shock tube problem, the Shu–Osher problem, and the Sedov blast wave problem showed the ability of the method to capture shocks robustly while localizing the dissipation to regions near shocks. The WCHR6 scheme was shown to have much better dispersion and dissipation characteristics compared to the other schemes considered. The boundary schemes were also shown to be stable and accurate with appropriate boundary treatments for problems having features leaving the computational domain. The 2D shock interaction with a strong vortex showed the ability of the scheme to capture shocks with complex structures and large pressure variations. The robustness of the scheme while still being minimally dissipative was demonstrated in the double Mach reflection problem where the strong Mach 10 shock is captured robustly while the Kelvin–Helmholtz instability is minimally dissipated. The 3D Taylor–Green vortex problem highlighted the minimal dissipation characteristic of the scheme for a 3D problem with a large range of scales. Finally, the compressible homogeneous isotropic turbulence test case showed that the WCHR6 scheme was capable of capturing eddy shocklets randomly distributed in the turbulent field while still being minimally dissipative for both the solenoidal and dilatational motions.

Acknowledgments

The code for all the 2D and 3D simulations in this paper is written in the high-level programming language Regent that uses the Legion tasking model developed at Stanford University. We acknowledge the support of Dr. Alex Aiken and Wonchan Lee with the task-based parallel programming in Regent and the Legion runtime system. It is our

pleasure to acknowledge the benefits to this paper resulting from the comments of an anonymous referee who insisted on the Sedov blast wave and double Mach reflection test cases. Additional robust treatment was required to improve the scheme for these strong shock cases and resulted in an improved scheme, but this has an insignificant effect on the performance for Taylor–Green vortex and compressible homogeneous isotropic turbulence test cases.

Appendix A. Nonlinear weights

Nonlinear weights are essential for nonlinear schemes such as WENO, WCNS, and WCHR schemes to capture discontinuities without spurious oscillations. Different forms of linear weights are discussed in this section.

Appendix A.1. Classical upwind-biased (JS) nonlinear weights

For a weighted scheme with four sub-stencils, the classical JS nonlinear weighting method designed by Jiang and Shu [23] only assigns weights to the three upwind stencils and are therefore upwind-biased. The JS nonlinear weights ω_k^{JS} are given by:

$$\omega_k^{\text{JS}} = \frac{\alpha_k^{\text{JS}}}{\sum_{k=0}^2 \alpha_k^{\text{JS}}}, \quad \alpha_k^{\text{JS}} = \frac{d_k^{\text{upwind}}}{(\beta_k + \epsilon)^p}, \quad k = 0, 1, 2, \quad (\text{A.1})$$

$$\omega_3^{\text{JS}} = 0, \quad (\text{A.2})$$

where p is a positive integer and $\epsilon = 1.0\text{e-}15$ is a very small number to prevent division by zero. β_k are smoothness indicators and are defined as:

$$\beta_k = \sum_{l=1}^2 \int_{x_{j-\frac{1}{2}}}^{x_{j+\frac{1}{2}}} \Delta x^{2l-1} \left(\frac{\partial^l}{\partial x^l} \tilde{u}^{(k)}(x) \right)^2 dx, \quad k = 0, 1, 2, \quad (\text{A.3})$$

where $\tilde{u}^{(k)}(x)$ is the Lagrange interpolating polynomial from stencil S_k in figure 1 for WCNS and WCHR schemes. The integrated forms of the smoothness indicators are given by [48]:

$$\beta_0 = \frac{1}{3} [u_{j-2} (4u_{j-2} - 19u_{j-1} + 11u_j) + u_{j-1} (25u_{j-1} - 31u_j) + 10u_j^2], \quad (\text{A.4})$$

$$\beta_1 = \frac{1}{3} [u_{j-1} (4u_{j-1} - 13u_j + 5u_{j+1}) + 13u_j (u_j - u_{j+1}) + 4u_{j+1}^2], \quad (\text{A.5})$$

$$\beta_2 = \frac{1}{3} [u_j (10u_j - 31u_{j+1} + 11u_{j+2}) + u_{j+1} (25u_{j+1} - 19u_{j+2}) + 4u_{j+2}^2]. \quad (\text{A.6})$$

Appendix A.2. Improved upwind-biased (Z) nonlinear weights

The upwind-biased Z nonlinear weights designed by Borges et al. [3] improves the excessive dissipative nature of the JS nonlinear weights. The Z nonlinear weights ω_k^{Z} are given by:

$$\omega_k^{\text{Z}} = \frac{\alpha_k^{\text{Z}}}{\sum_{k=0}^2 \alpha_k^{\text{Z}}}, \quad \alpha_k^{\text{Z}} = d_k^{\text{upwind}} \left(1 + \left(\frac{\tau_5}{\beta_k + \epsilon} \right)^p \right), \quad k = 0, 1, 2, \quad (\text{A.7})$$

$$\omega_3^Z = 0, \quad (\text{A.8})$$

where $\tau_5 = |\beta_2 - \beta_0|$ is a reference smoothness indicator and p is a positive integer.

Appendix A.3. Localized dissipation (LD) nonlinear weights

The nonlinear LD interpolation designed by Wong and Lele [45] also assigns nonlinear weight to the downwind stencil besides the upwind ones that helps the nonlinear interpolation recovers the non-dissipative central interpolation in smooth regions of the solutions. The LD nonlinear weights ω_k^{LD} are given by:

$$\omega_k^{\text{LD}} = \begin{cases} \sigma \omega_k^{\text{upwind}} + (1 - \sigma) \omega_k^{\text{central}}, & \text{if } R_\tau > \alpha_{RL}^\tau, \\ \omega_k^{\text{central}}, & \text{otherwise,} \end{cases} \quad k = 0, 1, 2, 3, \quad (\text{A.9})$$

where $\omega_k^{\text{upwind}} = \omega_k^Z$ and $\omega_k^{\text{central}}$ is given by:

$$\omega_k^{\text{central}} = \frac{\alpha_k^{\text{central}}}{\sum_{k=0}^3 \alpha_k^{\text{central}}}, \quad \alpha_k^{\text{central}} = d_k^{\text{central}} \left(C + \left(\frac{\tau_6}{\beta_k + \epsilon} \right)^q \right), \quad k = 0, 1, 2, 3, \quad (\text{A.10})$$

where q is a positive integer, C is a positive constant, and β_3 is defined as:

$$\beta_3 = \sum_{l=1}^5 \int_{x_{j-\frac{1}{2}}}^{x_{j+\frac{1}{2}}} \Delta x^{2l-1} \left(\frac{\partial^l}{\partial x^l} \tilde{u}^{(6)}(x) \right)^2 dx, \quad (\text{A.11})$$

where $\tilde{u}^{(6)}(x)$ is the Lagrange interpolating polynomial from stencil S_{central} in figure 1. The integrated form of β_3 is given by [29]:

$$\begin{aligned} \beta_3 = \frac{1}{232243200} [& u_{j-2} (525910327u_{j-2} - 4562164630u_{j-1} + 7799501420u_j \\ & - 6610694540u_{j+1} + 2794296070u_{j+2} - 472758974u_{j+3}) \\ & + 5u_{j-1} (2146987907u_{j-1} - 7722406988u_j + 6763559276u_{j+1} - 2926461814u_{j+2} + 503766638u_{j+3}) \\ & + 20u_j (1833221603u_j - 3358664662u_{j+1} + 1495974539u_{j+2} - 263126407u_{j+3}) \\ & + 20u_{j+1} (1607794163u_{j+1} - 1486026707u_{j+2} + 268747951u_{j+3}) \\ & + 5u_{j+2} (1432381427u_{j+2} - 536951582u_{j+3}) + 263126407u_{j+3}^2]. \end{aligned} \quad (\text{A.12})$$

τ_6 is a reference smoothness indicator:

$$\tau_6 = |\beta_3 - \beta_{\text{avg}}|, \quad (\text{A.13})$$

where

$$\beta_{\text{avg}} = \frac{1}{8} (\beta_0 + 6\beta_1 + \beta_2). \quad (\text{A.14})$$

R_τ is a relative sensor to distinguish smooth and non-smooth regions and is defined as:

$$R_\tau = \frac{\tau_6}{\beta_{\text{avg}} + \epsilon}. \quad (\text{A.15})$$

α_{RL}^τ is a constant to determine the cut-off for the hybridization between upwind-biased and central nonlinear weights. $0 \leq \sigma \leq 1$ is a blending function that is close to one in regions near discontinuities and high wavenumber features. In this paper, the following form of σ is used:

$$\sigma_{j+\frac{1}{2}} = \max(\sigma_j, \sigma_{j+1}), \quad (\text{A.16})$$

where σ_j is defined as:

$$\sigma_j = \frac{|\Delta u_{j+\frac{1}{2}} - \Delta u_{j-\frac{1}{2}}|}{|\Delta u_{j+\frac{1}{2}}| + |\Delta u_{j-\frac{1}{2}}| + \epsilon}, \quad (\text{A.17})$$

$$\Delta u_{j+\frac{1}{2}} = u_{j+1} - u_j. \quad (\text{A.18})$$

Appendix B. Coefficients of explicit-compact interpolations (ECI)

Appendix B.1. Interior scheme

The coefficients of the linear interpolations from S_{upwind} (equation (24)) and S_{central} (equation (25)) are given by:

$$\begin{aligned} \alpha^{\text{upwind}} &= -\frac{5(\xi-1)(13\xi-7)}{8(\xi+5)(2\xi-1)}, & \beta^{\text{upwind}} &= \frac{53\xi-5}{8(\xi+5)}, & \gamma^{\text{upwind}} &= -\frac{5(\xi-1)(5\xi-2)}{8(\xi+5)(2\xi-1)}, \\ a^{\text{upwind}} &= \frac{3(8\xi-5)}{64(\xi+5)}, & b^{\text{upwind}} &= -\frac{5(84\xi^2-103\xi+31)}{64(\xi+5)(2\xi-1)}, & c^{\text{upwind}} &= \frac{5(68\xi^2+11\xi-25)}{64(\xi+5)(2\xi-1)}, \\ d^{\text{upwind}} &= \frac{5(52\xi^2-11\xi-5)}{64(\xi+5)(2\xi-1)}, & e^{\text{upwind}} &= -\frac{5(4\xi-3)(5\xi-2)}{64(\xi+5)(2\xi-1)}, \end{aligned} \quad (\text{B.1})$$

and

$$\begin{aligned} \alpha^{\text{central}} &= -\frac{45(\xi-1)}{16(\xi+5)}, & \beta^{\text{central}} &= \frac{53\xi-5}{8(\xi+5)}, & \gamma^{\text{central}} &= -\frac{45(\xi-1)}{16(\xi+5)}, \\ a^{\text{central}} &= \frac{3(8\xi-5)}{128(\xi+5)}, & b^{\text{central}} &= -\frac{5(52\xi-37)}{128(\xi+5)}, & c^{\text{central}} &= \frac{75(2\xi+1)}{64(\xi+5)}, \\ d^{\text{central}} &= \frac{75(2\xi+1)}{64(\xi+5)}, & e^{\text{central}} &= -\frac{5(52\xi-37)}{128(\xi+5)}, & f^{\text{central}} &= \frac{3(8\xi-5)}{128(\xi+5)}. \end{aligned} \quad (\text{B.2})$$

Appendix B.2. Boundary scheme

The coefficients of the left-biased interpolations (equations (29) and (30)) at the left boundary (LB) are given by:

$$\begin{aligned}
a^{\text{LB}} &= -\frac{8\xi_0 - 3}{4}, & b^{\text{LB}} &= \frac{8\xi_0 + 1}{4}, & c^{\text{LB}} &= -\frac{4\xi_0 - 1}{4}, \\
d^{\text{LB}} &= \frac{3}{4}, & e^{\text{LB}} &= \xi_0, & f^{\text{LB}} &= -\frac{8\xi_1 - 15}{8}, \\
g^{\text{LB}} &= \frac{12\xi_1 - 5}{4}, & h^{\text{LB}} &= -\frac{3(8\xi_1 - 1)}{8}, & i^{\text{LB}} &= \xi_1,
\end{aligned} \tag{B.3}$$

where ξ_0 and ξ_1 are two free parameters and the linear weights in equations (31) and (32) are given by:

$$d_0^{(5),\text{LB}} = \frac{56\xi_0 - 5}{24(24\xi_0 - 5)}, \quad d_1^{(5),\text{LB}} = \frac{5(104\xi_0 - 11)}{24(24\xi_0 - 5)}, \quad d_2^{(5),\text{LB}} = -\frac{5}{2(24\xi_0 - 5)}, \tag{B.4}$$

and

$$\begin{aligned}
d_0^{(6),\text{LB}} &= \frac{6560\xi_0\xi_1 + 552\xi_0 - 716\xi_1 - 75}{24(3648\xi_0\xi_1 + 376\xi_0 - 1080\xi_1 - 145)}, \\
d_1^{(6),\text{LB}} &= \frac{161984\xi_0\xi_1 + 15480\xi_0 - 20456\xi_1 - 2385}{48(3648\xi_0\xi_1 + 376\xi_0 - 1080\xi_1 - 145)}, \\
d_2^{(6),\text{LB}} &= -\frac{624\xi_1 + 90}{3648\xi_0\xi_1 + 376\xi_0 - 1080\xi_1 - 145}, \\
d_3^{(6),\text{LB}} &= \frac{488\xi_0 - 35}{16(3648\xi_0\xi_1 + 376\xi_0 - 1080\xi_1 - 145)}.
\end{aligned} \tag{B.5}$$

In the case of $\xi = \frac{2}{3}$, if the truncation errors of interpolations from stencils S_5^{LB} and S_5^{LB} are matched with those of S_{upwind} and S_{central} respectively, we will get:

$$\xi_0 = \frac{9}{152}, \quad \xi_1 = -\frac{14445}{171608}. \tag{B.6}$$

Therefore,

$$\begin{aligned}
a^{\text{LB}} &= \frac{12}{19}, & b^{\text{LB}} &= \frac{7}{19}, & c^{\text{LB}} &= \frac{29}{152}, & d^{\text{LB}} &= \frac{3}{4}, \\
e^{\text{LB}} &= \frac{9}{152}, & f^{\text{LB}} &= \frac{168105}{85804}, & g^{\text{LB}} &= -\frac{257845}{171608}, & h^{\text{LB}} &= \frac{13461}{21451}, \\
i^{\text{LB}} &= -\frac{14445}{171608},
\end{aligned} \tag{B.7}$$

and

$$d_0^{(5),\text{LB}} = \frac{1}{51}, \quad d_1^{(5),\text{LB}} = \frac{115}{408}, \quad d_2^{(5),\text{LB}} = \frac{95}{136}, \tag{B.8}$$

and

$$d_0^{(6),\text{LB}} = \frac{34531}{2811392}, \quad d_1^{(6),\text{LB}} = \frac{324345}{1405696}, \quad d_2^{(6),\text{LB}} = \frac{3465}{4624}, \quad d_3^{(6),\text{LB}} = \frac{1129}{147968}. \quad (\text{B.9})$$

The coefficients of the left-biased interpolations (equations (33) and (34)) at the right boundary (RB) are given by:

$$\begin{aligned} a^{\text{RB}} &= \xi_2, & b^{\text{RB}} &= -\frac{3(8\xi_2 - 1)}{8}, & c^{\text{RB}} &= \frac{12\xi_2 - 5}{4}, \\ d^{\text{RB}} &= -\frac{8\xi_2 - 15}{8}, & e^{\text{RB}} &= \frac{8\xi_3 + 1}{4}, & f^{\text{RB}} &= -\frac{8\xi_3 - 3}{4}, \\ g^{\text{RB}} &= \xi_3, & h^{\text{RB}} &= \frac{3}{4}, & i^{\text{RB}} &= -\frac{4\xi_3 - 1}{4}, \end{aligned} \quad (\text{B.10})$$

where ξ_2 and ξ_3 are two free parameters and the linear weights in equations (37) and (38) are given by:

$$\begin{aligned} d_0^{(5),\text{RB}} &= \frac{56\xi_3 - 5}{32(48\xi_2\xi_3 - 26\xi_2 + 8\xi_3 - 5)}, & d_1^{(5),\text{RB}} &= -\frac{76\xi_2 + 15}{4(48\xi_2\xi_3 - 26\xi_2 + 8\xi_3 - 5)}, \\ d_2^{(5),\text{RB}} &= \frac{1536\xi_2\xi_3 - 224\xi_2 + 200\xi_3 - 35}{32(48\xi_2\xi_3 - 26\xi_2 + 8\xi_3 - 5)}, \end{aligned} \quad (\text{B.11})$$

and

$$\begin{aligned} d_0^{(6),\text{RB}} &= \frac{488\xi_3 - 35}{16(3648\xi_2\xi_3 - 1080\xi_2 + 376\xi_3 - 145)}, \\ d_1^{(6),\text{RB}} &= -\frac{624\xi_2 + 90}{3648\xi_2\xi_3 - 1080\xi_2 + 376\xi_3 - 145}, \\ d_2^{(6),\text{RB}} &= \frac{161984\xi_2\xi_3 - 20456\xi_2 + 15480\xi_3 - 2385}{48(3648\xi_2\xi_3 - 1080\xi_2 + 376\xi_3 - 145)}, \\ d_3^{(6),\text{RB}} &= \frac{6560\xi_2\xi_3 - 716\xi_2 + 552\xi_3 - 75}{24(3648\xi_2\xi_3 - 1080\xi_2 + 376\xi_3 - 145)}. \end{aligned} \quad (\text{B.12})$$

In the case of $\xi = \frac{2}{3}$, if the truncation errors of interpolations from stencils S_5^{RB} and S_5^{RB} are matched with those of S_{upwind} and S_{central} respectively, we will get:

$$\xi_2 = -\frac{3182085}{37433632} - \frac{45\sqrt{723535913}}{37433632}, \quad \xi_3 = -\frac{9\sqrt{723535913}}{7659176} + \frac{96676}{957397}. \quad (\text{B.13})$$

Therefore,

$$\begin{aligned}
a^{\text{RB}} &= -\frac{3182085}{37433632} - \frac{45\sqrt{723535913}}{37433632}, & b^{\text{RB}} &= \frac{135\sqrt{723535913}}{37433632} + \frac{23583867}{37433632}, \\
c^{\text{RB}} &= -\frac{56338295}{37433632} - \frac{135\sqrt{723535913}}{37433632}, & d^{\text{RB}} &= \frac{45\sqrt{723535913}}{37433632} + \frac{73370145}{37433632}, \\
e^{\text{RB}} &= -\frac{9\sqrt{723535913}}{3829588} + \frac{1730805}{3829588}, & f^{\text{RB}} &= \frac{9\sqrt{723535913}}{3829588} + \frac{2098783}{3829588}, \\
g^{\text{RB}} &= -\frac{9\sqrt{723535913}}{7659176} + \frac{96676}{957397}, & h^{\text{RB}} &= \frac{3}{4}, \\
i^{\text{RB}} &= \frac{9\sqrt{723535913}}{7659176} + \frac{570693}{3829588}, & &
\end{aligned} \tag{B.14}$$

and

$$\begin{aligned}
d_0^{(5),\text{RB}} &= -\frac{135353}{41283072} + \frac{35\sqrt{723535913}}{41283072}, & d_1^{(5),\text{RB}} &= -\frac{145\sqrt{723535913}}{82566144} + \frac{74237155}{82566144}, \\
d_2^{(5),\text{RB}} &= \frac{25\sqrt{723535913}}{27522048} + \frac{2866565}{27522048}, & &
\end{aligned} \tag{B.15}$$

and

$$\begin{aligned}
d_0^{(6),\text{RB}} &= -\frac{2038531}{157733888} + \frac{95\sqrt{723535913}}{157733888}, & d_1^{(6),\text{RB}} &= -\frac{95\sqrt{723535913}}{39433472} + \frac{32791565}{39433472}, \\
d_2^{(6),\text{RB}} &= \frac{135\sqrt{723535913}}{78866944} + \frac{13590345}{78866944}, & d_3^{(6),\text{RB}} &= \frac{15\sqrt{723535913}}{157733888} + \frac{1425469}{157733888}.
\end{aligned} \tag{B.16}$$

Appendix C. Block-tridiagonal matrix solution algorithm

Appendix C.1. Matrix solution algorithm

Consider a block tridiagonal matrix system $\mathbf{A}\mathbf{x} = \mathbf{b}$ given by:

$$\mathbf{A} = \begin{pmatrix} \beta_1 & \gamma_1 & & & \\ \alpha_2 & \beta_2 & \gamma_2 & & \\ & & \ddots & & \\ & & & \alpha_{N-1} & \beta_{N-1} & \gamma_{N-1} \\ & & & & \alpha_N & \beta_N \end{pmatrix}, \tag{C.1}$$

$$\mathbf{x} = \begin{pmatrix} \mathbf{x}_1 \\ \mathbf{x}_2 \\ \vdots \\ \mathbf{x}_{N-1} \\ \mathbf{x}_N \end{pmatrix}, \quad \mathbf{b} = \begin{pmatrix} \mathbf{b}_1 \\ \mathbf{b}_2 \\ \vdots \\ \mathbf{b}_{N-1} \\ \mathbf{b}_N \end{pmatrix}, \tag{C.2}$$

where α_i , β_i , and γ_i are $B_s \times B_s$ matrix blocks. \mathbf{x}_i and \mathbf{b}_i are $B_s \times 1$ vector elements of the solution and the RHS vectors respectively.

For the resulting block-tridiagonal system, we use derive a block version of the Thomas algorithm with a forward elimination step:

$$\Delta_i = [\beta_i - \alpha_i \Delta_{i-1} \gamma_{i-1}]^{-1}, \quad (\text{C.3})$$

$$\hat{\mathbf{b}}_i = -\mathbf{b}_i - \alpha_i \Delta_{i-1} \hat{\mathbf{b}}_{i-1}, \quad (\text{C.4})$$

and a back substitution step:

$$\mathbf{x}_i = -\Delta_i [\hat{\mathbf{b}}_i + \gamma_i \mathbf{x}_{i+1}]. \quad (\text{C.5})$$

For periodic problems resulting in a cyclic block tridiagonal matrix \mathbf{A}_p , we use the Sherman-Morrison low rank correction given by:

$$\mathbf{A}_p^{-1} = (\mathbf{A} + \mathbf{U}\mathbf{V}^T)^{-1} = \mathbf{A}^{-1} - \mathbf{A}^{-1}\mathbf{U} (\mathbf{I} + \mathbf{V}^T \mathbf{A}^{-1} \mathbf{U})^{-1} \mathbf{V}^T \mathbf{A}^{-1}, \quad (\text{C.6})$$

where

$$\mathbf{A}_p = \begin{pmatrix} \tilde{\beta}_1 & \tilde{\gamma}_1 & & & \tilde{\alpha}_1 \\ \tilde{\alpha}_2 & \tilde{\beta}_2 & \tilde{\gamma}_2 & & \\ & & \ddots & & \\ & & \tilde{\alpha}_{N-1} & \tilde{\beta}_{N-1} & \tilde{\gamma}_{N-1} \\ \tilde{\gamma}_N & & & \tilde{\alpha}_N & \tilde{\beta}_N \end{pmatrix}, \quad (\text{C.7})$$

$$\mathbf{A} = \begin{pmatrix} \tilde{\alpha}_1 + \tilde{\beta}_1 & \tilde{\gamma}_1 & & & \\ \tilde{\alpha}_2 & \tilde{\beta}_2 & \tilde{\gamma}_2 & & \\ & & \ddots & & \\ & & \tilde{\alpha}_{N-1} & \tilde{\beta}_{N-1} & \tilde{\gamma}_{N-1} \\ & & & \tilde{\alpha}_N & \tilde{\beta}_N + \tilde{\gamma}_N \end{pmatrix}, \quad (\text{C.8})$$

and \mathbf{U} and \mathbf{V} are given by:

$$\mathbf{U} = \begin{pmatrix} -\tilde{\alpha}_1 \\ \mathbf{0} \\ \vdots \\ \mathbf{0} \\ \tilde{\gamma}_N \end{pmatrix}, \quad \mathbf{V} = \begin{pmatrix} \mathbf{I} \\ \mathbf{0} \\ \vdots \\ \mathbf{0} \\ -\mathbf{I} \end{pmatrix}. \quad (\text{C.9})$$

The pseudo code for the block-tridiagonal algorithm including the Sherman-Morrison correction is given in algorithm 1.

Appendix C.2. Application to compact interpolation

The compact interpolations with characteristic decomposition used in this paper result in block tridiagonal systems as in equation (C.2) for non-periodic problems or equation (C.7) for periodic problems. In both cases, each block is a 5×5 matrix that is a scaled version of the Jacobian matrix of the fluxes with respect to primitive variables.

Algorithm 1 Pseudo code for the block-tridiagonal matrix solution algorithm. Internal variables required are Δ_i (memory cost of $B_s^2 N$) and $\hat{\mathbf{b}}_i$ (memory cost of $B_s N$) and periodic problems require $\hat{\mathbf{U}}_i$ (memory cost of $B_s^2 N$) in addition. B_s is the size of each block in the system. The solution can be computed in-place by replacing $\hat{\mathbf{b}}_i$ and \mathbf{x}_i by \mathbf{b}_i .

```

if periodic then
   $\beta_1 \leftarrow \tilde{\alpha}_1 + \tilde{\beta}_1$ 
   $\gamma_1 \leftarrow \tilde{\gamma}_1$ 
  for  $i = 2, 3, \dots, N - 1$  do
     $\alpha_i \leftarrow \tilde{\alpha}_i$ 
     $\beta_i \leftarrow \tilde{\beta}_i$ 
     $\gamma_i \leftarrow \tilde{\gamma}_i$ 
  end for
   $\alpha_N \leftarrow \tilde{\alpha}_N$ 
   $\beta_N \leftarrow \tilde{\beta}_N + \tilde{\gamma}_N$ 
end if
 $\Delta_1 = \beta_1^{-1}$ 
 $\hat{\mathbf{b}}_1 = -\mathbf{b}_1$ 
if periodic then
   $\hat{\mathbf{U}}_1 = \tilde{\alpha}_1$ 
end if
for  $i = 2, 3, \dots, N$  do
   $\Delta_i = [\beta_i - \alpha_i \Delta_{i-1} \gamma_{i-1}]^{-1}$ 
   $\hat{\mathbf{b}}_i = -\mathbf{b}_i - \alpha_i \Delta_{i-1} \hat{\mathbf{b}}_{i-1}$ 
  if periodic then
     $\hat{\mathbf{U}}_i = -\alpha_i \Delta_{i-1} \hat{\mathbf{U}}_{i-1}$ 
  end if
end for
if periodic then
   $\hat{\mathbf{U}}_N \leftarrow -\tilde{\gamma}_N + \hat{\mathbf{U}}_N$ 
end if
 $\mathbf{x}_N = -\Delta_N \hat{\mathbf{b}}_N$ 
if periodic then
   $\hat{\mathbf{U}}_N \leftarrow -\Delta_N \hat{\mathbf{U}}_N$ 
end if
for  $i = N - 1, N - 2, \dots, 1$  do
   $\mathbf{x}_i = -\Delta_i [\hat{\mathbf{b}}_i + \gamma_i \mathbf{x}_{i+1}]$ 
  if periodic then
     $\hat{\mathbf{U}}_i \leftarrow -\Delta_i [\hat{\mathbf{U}}_i + \gamma_i \hat{\mathbf{U}}_{i+1}]$ 
  end if
end for
if periodic then
   $M = I + \hat{\mathbf{U}}_1 - \hat{\mathbf{U}}_N$ 
   $\mathbf{y} = M^{-1}(\mathbf{x}_1 - \mathbf{x}_N)$ 
  for  $i = 1, 2, \dots, N$  do
     $\mathbf{x}_i \leftarrow \mathbf{x}_i - \hat{\mathbf{U}}_i \mathbf{y}$ 
  end for
end if

```

The Jacobian matrix forming each block in the x direction interpolation of a 3D problem is given by:

$$\begin{pmatrix} 0 & -\frac{\rho c}{2} & 0 & 0 & \frac{1}{2} \\ 1 & 0 & 0 & 0 & -\frac{1}{c^2} \\ 0 & 0 & 1 & 0 & 0 \\ 0 & 0 & 0 & 1 & 0 \\ 0 & \frac{\rho c}{2} & 0 & 0 & \frac{1}{2} \end{pmatrix}, \quad (\text{C.10})$$

where the rows correspond to the primitive variables (ρ, u, v, w, p) .

Given this structure, we can decouple the third and fourth rows (corresponding to v and w) and split the problem into a 3×3 block tridiagonal system corresponding to (ρ, u, p) and separate independent tridiagonal systems for v and w . In the y direction, the u and w interpolations are independent and in the z direction, the u and v interpolations are independent.

The reduced 3×3 block tridiagonal system may be solved using the algorithm described in section [Appendix C.1](#). The cost of the block tridiagonal algorithm scales as $\mathcal{O}(B_s^3 N)$ where B_s is the block size and N is the number of diagonal blocks in the system. Reducing the block size from 5 to 3 would then reduce the operation count by a factor of ≈ 4.6 . The tridiagonal systems for the two transverse velocity components may be solved using the Thomas algorithm or a symbolic factorization based algorithm [\[33\]](#).

Appendix D. Relation between compact finite difference schemes and flux difference form for provable discrete conservation

Appendix D.1. Formulation

Given a scalar hyperbolic equation of conservative variable $u(x, t)$ of the form:

$$\frac{\partial u}{\partial t} + \frac{\partial F(u)}{\partial x} = 0, \quad (\text{D.1})$$

defined in the domain $x \in [x_a, x_b]$. We can get a semi-discretized form using the finite difference formalism as:

$$\frac{\partial u_j}{\partial t} + \frac{\partial F}{\partial x} \Big|_{x=x_j} = 0, \quad (\text{D.2})$$

where $u_j(t) = u(x_j, t)$ and is available at discrete points $x_j = x_a + (1/2 + j)\Delta x$, $\forall j \in \{0, 1, \dots, N-1\}$.

Let us define $h(x, t; \Delta x)$ implicitly as:

$$F(u(x, t)) = F(x, t) = \frac{1}{\Delta x} \int_{x-\frac{\Delta x}{2}}^{x+\frac{\Delta x}{2}} h(\xi, t; \Delta x) d\xi. \quad (\text{D.3})$$

Equation [\(D.2\)](#) can then be rewritten as:

$$\frac{du_j}{dt} + \frac{1}{\Delta x} \left[h\left(x_{j+\frac{1}{2}}, t; \Delta x\right) - h\left(x_{j-\frac{1}{2}}, t; \Delta x\right) \right] = 0, \quad (\text{D.4})$$

or shortened as:

$$\frac{du_j}{dt} + \frac{1}{\Delta x} \left(h_{j+\frac{1}{2}} - h_{j-\frac{1}{2}} \right) = 0, \quad (\text{D.5})$$

with the definition $h\left(x_{j+\frac{1}{2}}, t; \Delta x\right) = h_{j+\frac{1}{2}}$. We may also define the primitive function of $h(x, t; \Delta x)$:

$$H(x, t; \Delta x) = \int_{x_a}^x h(\xi, t; \Delta x) d\xi. \quad (\text{D.6})$$

Therefore,

$$\begin{aligned} H(x_{j+\frac{1}{2}}, t; \Delta x) &= \int_{x_a}^{x_{j+\frac{1}{2}}} h(\xi, t; \Delta x) d\xi \\ &= \Delta x \sum_{i=0}^j F(x_i, t) \\ &= \Delta x \sum_{i=0}^j F_i. \end{aligned} \quad (\text{D.7})$$

Also,

$$H'\left(x_{j+\frac{1}{2}}, t; \Delta x\right) = h\left(x_{j+\frac{1}{2}}, t; \Delta x\right). \quad (\text{D.8})$$

Or for simplification, if we define $H'_{j+\frac{1}{2}} = H'\left(x_{j+\frac{1}{2}}, t; \Delta x\right)$, we get:

$$H'_{j+\frac{1}{2}} = h_{j+\frac{1}{2}}. \quad (\text{D.9})$$

Now, let us denote a p^{th} order numerical representation of $H'_{j+\frac{1}{2}}$ by $\widehat{F}_{j+\frac{1}{2}} \approx h_{j+\frac{1}{2}} + \mathcal{O}(\Delta x^p) = H'_{j+\frac{1}{2}} + \mathcal{O}(\Delta x^p)$, which is a reconstructed form of the flux. We can get such an approximation using a p^{th} order compact finite difference scheme for $H'_{j+\frac{1}{2}}$ in general form:

$$\begin{aligned} \alpha \widehat{F}_{j-\frac{1}{2}} + \beta \widehat{F}_{j+\frac{1}{2}} + \gamma \widehat{F}_{j+\frac{3}{2}} &= \\ \frac{1}{\Delta x} &\left(a_{-\frac{3}{2}} H_{j-\frac{3}{2}} + a_{-1} H_{j-1} + a_{-\frac{1}{2}} H_{j-\frac{1}{2}} + a_0 H_j \right. \\ &\left. + a_{\frac{1}{2}} H_{j+\frac{1}{2}} + a_1 H_{j+1} + a_{\frac{3}{2}} H_{j+\frac{3}{2}} + a_2 H_{j+2} + a_{\frac{5}{2}} H_{j+\frac{5}{2}} \right). \end{aligned} \quad (\text{D.10})$$

Using equation (D.7), we get:

$$\begin{aligned} \alpha \widehat{F}_{j-\frac{1}{2}} + \beta \widehat{F}_{j+\frac{1}{2}} + \gamma \widehat{F}_{j+\frac{3}{2}} &= \\ \frac{1}{\Delta x} &\left[\left(a_{-\frac{3}{2}} + a_{-\frac{1}{2}} + a_{\frac{1}{2}} + a_{\frac{3}{2}} + a_{\frac{5}{2}} \right) H_{j-\frac{3}{2}} + (a_{-1} + a_0 + a_1 + a_2) H_{j-1} \right. \\ &+ a_{-\frac{1}{2}} F_{j-1} + a_0 F_{j-\frac{1}{2}} + a_{\frac{1}{2}} (F_{j-1} + F_j) + a_1 \left(F_{j-\frac{1}{2}} + F_{j+\frac{1}{2}} \right) \\ &\left. + a_{\frac{3}{2}} (F_{j-1} + F_j + F_{j+1}) + a_2 \left(F_{j-\frac{1}{2}} + F_{j+\frac{1}{2}} + F_{j+\frac{3}{2}} \right) + a_{\frac{5}{2}} (F_{j-1} + F_j + F_{j+1} + F_{j+2}) \right]. \end{aligned} \quad (\text{D.11})$$

After re-arranging,

$$\begin{aligned}
& \alpha \widehat{F}_{j-\frac{1}{2}} + \beta \widehat{F}_{j+\frac{1}{2}} + \gamma \widehat{F}_{j+\frac{3}{2}} \\
&= (a_{-1} + a_0 + a_1 + a_2) H_{j-1} + (a_0 + a_1 + a_2) F_{j-\frac{1}{2}} + (a_1 + a_2) F_{j+\frac{1}{2}} + a_2 F_{j+\frac{3}{2}} \\
&+ \left(a_{-\frac{3}{2}} + a_{-\frac{1}{2}} + a_{\frac{1}{2}} + a_{\frac{3}{2}} + a_{\frac{5}{2}} \right) H_{j-\frac{3}{2}} + \left(a_{-\frac{1}{2}} + a_{\frac{1}{2}} + a_{\frac{3}{2}} + a_{\frac{5}{2}} \right) F_{j-1} \\
&+ \left(a_{\frac{1}{2}} + a_{\frac{3}{2}} + a_{\frac{5}{2}} \right) F_j + \left(a_{\frac{3}{2}} + a_{\frac{5}{2}} \right) F_{j+1} + a_{\frac{5}{2}} F_{j+2}.
\end{aligned} \tag{D.12}$$

If $(a_{-1} + a_0 + a_1 + a_2) = 0$ and $\left(a_{-\frac{3}{2}} + a_{-\frac{1}{2}} + a_{\frac{1}{2}} + a_{\frac{3}{2}} + a_{\frac{5}{2}} \right) = 0$ which is always true for a central scheme, we get a compact stencil representation of the reconstructed flux as:

$$\begin{aligned}
\alpha \widehat{F}_{j-\frac{1}{2}} + \beta \widehat{F}_{j+\frac{1}{2}} + \gamma \widehat{F}_{j+\frac{3}{2}} &= (a_0 + a_1 + a_2) F_{j-\frac{1}{2}} + (a_1 + a_2) F_{j+\frac{1}{2}} + a_2 F_{j+\frac{3}{2}} \\
&+ \left(a_{-\frac{1}{2}} + a_{\frac{1}{2}} + a_{\frac{3}{2}} + a_{\frac{5}{2}} \right) F_{j-1} \\
&+ \left(a_{\frac{1}{2}} + a_{\frac{3}{2}} + a_{\frac{5}{2}} \right) F_j + \left(a_{\frac{3}{2}} + a_{\frac{5}{2}} \right) F_{j+1} + a_{\frac{5}{2}} F_{j+2} \\
&= \widehat{a}_{-1} F_{j-1} + \widehat{a}_{-\frac{1}{2}} F_{j-\frac{1}{2}} + \widehat{a}_0 F_j + \widehat{a}_{\frac{1}{2}} F_{j+\frac{1}{2}} + \widehat{a}_1 F_{j+1} + \widehat{a}_{\frac{3}{2}} F_{j+\frac{3}{2}} \\
&+ \widehat{a}_2 F_{j+2},
\end{aligned} \tag{D.13}$$

with $\widehat{a}_{-1} = \left(a_{-\frac{1}{2}} + a_{\frac{1}{2}} + a_{\frac{3}{2}} + a_{\frac{5}{2}} \right)$, $\widehat{a}_0 = \left(a_{\frac{1}{2}} + a_{\frac{3}{2}} + a_{\frac{5}{2}} \right)$, $\widehat{a}_1 = \left(a_{\frac{3}{2}} + a_{\frac{5}{2}} \right)$, $\widehat{a}_2 = a_{\frac{5}{2}}$, $\widehat{a}_{-\frac{1}{2}} = (a_0 + a_1 + a_2)$, $\widehat{a}_{\frac{1}{2}} = (a_1 + a_2)$, and $\widehat{a}_{\frac{3}{2}} = a_2$.

With this p^{th} order approximation of $h_{j+\frac{1}{2}}$, we can solve the original conservation law in the conservation form as:

$$\frac{\partial u_j}{\partial t} + \frac{1}{\Delta x} \left(\widehat{F}_{j+\frac{1}{2}} - \widehat{F}_{j-\frac{1}{2}} \right) = 0. \tag{D.14}$$

If we define the flux difference form for the numerical approximation of derivative:

$$\left. \frac{\partial \widehat{F}}{\partial x} \right|_{x=x_j} = \widehat{F}'_j = \frac{1}{\Delta x} \left(\widehat{F}_{j+\frac{1}{2}} - \widehat{F}_{j-\frac{1}{2}} \right). \tag{D.15}$$

For a central scheme with $\alpha = \gamma$, $a_0 = -a_1$, $a_{-1} = -a_2$, $a_{\frac{1}{2}} = 0$, $a_{-\frac{1}{2}} = -a_{\frac{3}{2}}$, and $a_{-\frac{3}{2}} = -a_{\frac{5}{2}}$, it can be easily proven that:

$$\begin{aligned}
& \alpha \widehat{F}'_{j-1} + \beta \widehat{F}'_j + \alpha \widehat{F}'_{j+1} = \\
& \frac{1}{\Delta x} \left(-a_{\frac{5}{2}} F_{j-2} - a_2 F_{j-\frac{3}{2}} - a_{\frac{3}{2}} F_{j-1} - a_1 F_{j-\frac{1}{2}} + a_1 F_{j+\frac{1}{2}} + a_{\frac{3}{2}} F_{j+1} + a_2 F_{j+\frac{3}{2}} + a_{\frac{5}{2}} F_{j+2} \right).
\end{aligned} \tag{D.16}$$

Therefore, \widehat{F}'_j is p^{th} order approximation of F'_j with the same compact finite difference scheme used in equation (D.10) with the constraint that the scheme is central.

Flux reconstruction equation (D.13) relates any central finite difference scheme (compact or explicit) in form given by equation (D.16) to the flux difference form (equation (D.15)). For instance, the flux reconstruction equation of the sixth order CMD

scheme (equation (2)) is given by equation (40) and that of the sixth order CND scheme (equation (70)) is given by:

$$\frac{1}{5}\widehat{F}_{j-\frac{1}{2}} + \frac{3}{5}\widehat{F}_{j+\frac{1}{2}} + \frac{1}{5}\widehat{F}_{j+\frac{3}{2}} = \frac{1}{60}F_{j-1} + \frac{29}{60}F_j + \frac{29}{60}F_{j+1} + \frac{1}{60}F_{j+2}. \quad (\text{D.17})$$

To derive boundary closures for the flux reconstruction equation given by equation (D.13) such as the closure at the right boundary with $j = N - 1$, we can define a boundary flux reconstruction equation:

$$\alpha\widehat{F}_{j-\frac{1}{2}} + (\beta + \gamma)\widehat{F}_{j+\frac{1}{2}} = \dots \quad (\text{D.18})$$

where the right hand side is constructed based on a choice of cell node and midpoint flux values (either ghost cells or only interior). Then subtract equation (D.13) from the above and divide by Δx to get:

$$\alpha\widehat{F}'_{j-1} + \beta\widehat{F}'_j = \dots \quad (\text{D.19})$$

Given a desired truncation error, we can use the above equation and standard Taylor series expansion to get the coefficients of the right hand side terms in equation (D.18). For example, the flux reconstruction equation of $\widehat{F}_{j+\frac{1}{2}}$ for the right boundary (equation (42)), where $j = N - 1$, is given by:

$$\begin{aligned} \frac{9}{80}\widehat{F}_{j-\frac{1}{2}} + \frac{71}{80}\widehat{F}_{j+\frac{1}{2}} &= \frac{27233}{768000}F_{j-2} - \frac{80779}{336000}F_{j-\frac{3}{2}} + \frac{26353}{38400}F_{j-1} - \frac{7811}{8000}F_{j-\frac{1}{2}} + \frac{65699}{76800}F_j \\ &+ \frac{10989}{16000}F_{j+\frac{1}{2}} - \frac{9007}{192000}F_{j+1} - \frac{1633}{5376000}F_{j+2}. \end{aligned} \quad (\text{D.20})$$

Appendix D.2. Conservation

For a continuous problem in a non-periodic 1D domain, we have conservation of $u(x, t)$ given by:

$$\frac{\partial}{\partial t} \int_{x_0 - \frac{\Delta x}{2}}^{x_{N-1} + \frac{\Delta x}{2}} u(x, t) dx = F\left(x_0 - \frac{\Delta x}{2}, t\right) - F\left(x_{N-1} + \frac{\Delta x}{2}, t\right). \quad (\text{D.21})$$

Note that $x_0 - \Delta x/2$ and $x_{N-1} + \Delta x/2$ are the boundaries of the domain. If we choose a test function $\psi(x)$ given by:

$$\psi(x) = \sum_{j=0}^{N-1} \Delta x \cdot \delta(x - x_j), \quad (\text{D.22})$$

where $\delta(x)$ is the Dirac delta function, we have:

$$\frac{\partial}{\partial t} \int_{x_0 - \frac{\Delta x}{2}}^{x_{N-1} + \frac{\Delta x}{2}} \psi(x) u(x, t) dx = \Delta x \sum_{j=0}^{N-1} \frac{\partial u_j}{\partial t}. \quad (\text{D.23})$$

With the conservation form given by equation (D.14) after semi-discrete discretization, we have:

$$\begin{aligned} \frac{\partial}{\partial t} \int_{x_0 - \frac{\Delta x}{2}}^{x_{N-1} + \frac{\Delta x}{2}} \psi(x) u(x, t) dx &= \widehat{F}\left(x_{-\frac{1}{2}}, t\right) - \widehat{F}\left(x_{N-\frac{1}{2}}, t\right) \\ &= \widehat{F}\left(x_0 - \frac{\Delta x}{2}, t\right) - \widehat{F}\left(x_{N-1} + \frac{\Delta x}{2}, t\right). \end{aligned} \quad (\text{D.24})$$

Hence, the conservation form given by equation (D.14) guarantees discrete conservation under the test function $\psi(x)$. This form also proves that central compact or explicit finite difference schemes are discretely conservative for a periodic domain.

The main benefit of the conservation form and the corresponding flux reconstruction form of compact finite difference schemes, however, is the ability to derive boundary closures for compact finite difference schemes so that discrete conservation is guaranteed. The reconstruction form also has potential to allow the use of compact finite difference schemes with adaptive mesh refinement in order to get conservation across mesh levels with appropriately derived boundary schemes.

Appendix E. HLLC, HLL, and HLLC-HLL Riemann solvers

The flux in the x direction from the HLLC Riemann solver, \mathbf{F}_{HLLC} , for a 3D problem is given by:

$$\mathbf{F}_{\text{HLLC}} = \frac{1 + \text{sign}(s_*)}{2} [\mathbf{F}(\mathbf{Q}_L) + s_- (\mathbf{Q}_{*L} - \mathbf{Q}_L)] + \frac{1 - \text{sign}(s_*)}{2} [\mathbf{F}(\mathbf{Q}_R) + s_+ (\mathbf{Q}_{*R} - \mathbf{Q}_R)], \quad (\text{E.1})$$

where L and R are the left and right states respectively, and \mathbf{Q}_L and \mathbf{Q}_R are the corresponding conservative variable vectors. With $K = L$ or R , the star state is defined as:

$$\mathbf{Q}_{*K} = \chi_{*K} \begin{bmatrix} \rho_K \\ \rho_K s_* \\ \rho_K v_K \\ \rho_K w_K \\ E_k + (s_* - u_K) \left(\rho_K s_* + \frac{p_K}{s_K - u_K} \right) \end{bmatrix}, \quad (\text{E.2})$$

where

$$\chi_{*K} = \frac{s_K - u_K}{s_K - s_*}. \quad (\text{E.3})$$

We use the waves speeds suggested by Einfeldt et al. [10]:

$$s_- = \min(0, s_L), \quad s_+ = \max(0, s_R), \quad (\text{E.4})$$

and

$$s_L = \min(\bar{u} - \bar{c}, u_L - c_L), \quad s_R = \max(\bar{u} + \bar{c}, u_R + c_R), \quad (\text{E.5})$$

where \bar{u} and \bar{c} are the averages from the left and right states. Roe averages are used in this paper. Following Batten et al. [1], the wave speed for the star state is given by:

$$s_* = \frac{p_R - p_L + \rho_L u_L (s_L - u_L) - \rho_R u_R (s_R - u_R)}{\rho_L (s_L - u_L) - \rho_R (s_R - u_R)}. \quad (\text{E.6})$$

The flux from the HLL Riemann solver proposed by Harten et al. [16], \mathbf{F}_{HLL} , is given by:

$$\mathbf{F}_{\text{HLL}} = \begin{cases} \mathbf{F}(\mathbf{Q}_L), & \text{if } s_L \geq 0, \\ \frac{s_R \mathbf{F}(\mathbf{Q}_L) - s_L \mathbf{F}(\mathbf{Q}_R) + s_R s_L (\mathbf{Q}_R - \mathbf{Q}_L)}{s_R - s_L} & \text{if } s_L \leq 0 \leq s_R, \\ \mathbf{F}(\mathbf{Q}_R), & \text{if } s_R \leq 0. \end{cases} \quad (\text{E.7})$$

The hybrid flux in the x direction from the HLLC-HLL Riemann solver proposed by Huang et al. [21], $\mathbf{F}_{\text{HLLC-HLL}}$, for a 3D problem is given by:

$$\mathbf{F}_{\text{HLLC-HLL}} = \Theta \mathbf{F}_{\text{HLLC}} + (\mathbf{I} - \Theta) \mathbf{F}_{\text{HLL}}, \quad (\text{E.8})$$

where

$$\Theta = \begin{pmatrix} \tilde{\alpha}_1 & 0 & 0 & 0 & 0 \\ 0 & 1 & 0 & 0 & 0 \\ 0 & 0 & \tilde{\alpha}_1 & 0 & 0 \\ 0 & 0 & 0 & \tilde{\alpha}_1 & 0 \\ 0 & 0 & 0 & 0 & 1 \end{pmatrix}, \quad (\text{E.9})$$

and \mathbf{I} is the identity matrix. The weight, $\tilde{\alpha}_1 \in [0, 1]$, suggested by Huang et al. [21] is used:

$$\alpha_1 = \begin{cases} 1, & \text{if } |\mathbf{u}_R - \mathbf{u}_L| < \epsilon, \\ \frac{|u_R - u_L|}{|\mathbf{u}_R - \mathbf{u}_L|}, & \text{otherwise,} \end{cases} \quad (\text{E.10})$$

$$\alpha_2 = \sqrt{1 - \alpha_1^2}, \quad (\text{E.11})$$

$$\tilde{\alpha}_1 = \frac{1}{2} + \frac{1}{2} \frac{\alpha_1}{\alpha_1 + \alpha_2}. \quad (\text{E.12})$$

$\epsilon = 1.0\text{e-}15$ is the usual small constant close to machine epsilon. $\tilde{\alpha}_1$ is designed in the way such that when the shock normal direction is aligned with the grid surface normal direction, the hybrid flux is purely the HLLC flux. When the shock normal direction is perpendicular to the surface normal direction, HLL flux adds dissipation by sharing the same weight as the HLLC flux. In 1D problems, the HLLC-HLL Riemann solver is reduced to the regular HLLC Riemann solver since the shock normal direction is always perpendicular to the grid surface normal.

Appendix F. Effect of postprocessing pipeline for velocity gradient statistics

Statistics of velocity gradient quantities like vorticity or dilatation are important in the analysis of turbulent flows. Any field with a power law energy spectrum exponent of < 2 has a gradient power spectrum that grows with the wavenumber, which is the case for velocity fields in turbulent flows. This amplifies the sensitivity of gradient statistics to the derivative scheme used to compute velocity gradients from the primitive velocity fields. In this paper, we use Fourier spectral derivatives which are exact up to the Nyquist wavenumber assuming that the solution represented on the grid is not aliased. The results here, as a result, are different from some previously published results. For the compressible homogeneous isotropic turbulence case presented in section 3.11, we

present our results for the DNS reference solution using different postprocessing derivative schemes. We also compare them to previously published results of Johnsen et al. [24].

Figure F.36 shows the velocity statistics postprocessed using different derivative schemes. All results are obtained by spectrally filtering the velocity fields and then downsampling from the DNS resolution of 512^3 down to 64^3 . The derivative operators are constructed on the downsampled 64^3 grid and applied using the periodic boundary conditions of the problem. From figure 36(b), we see that the velocity variance is the same for all the cases and match the results of Johnsen et al. [24]. Figure 36(b) shows the enstrophy computed with different derivative schemes. From this, the effect of the postprocessing pipeline is evident. Using spectral derivatives which is the most accurate in the high wavenumber region has the highest enstrophy. For the other derivative schemes, the lower order derivatives capture much lower enstrophy. Also, compact derivatives are better than their explicit counterparts for the same order or accuracy. All of these results are in line with the modified wavenumbers of each derivative scheme. The same is true for the dilatation variance plotted in figure 36(c). The plots also show the results of Johnsen et al. [24] which are closest to the results using sixth order explicit finite difference. It was also confirmed by Larsson⁷ (one of the authors of Johnsen et al. [24]) that the sixth order explicit finite difference scheme was used for postprocessing. We see some difference between the sixth order explicit derivatives and the results of Johnsen et al. [24] in the dilatation variance for $t/\tau < 1$. Since the initial conditions are solenoidal and generated randomly following a prescribed spectrum, the dilatation variance is sensitive to the initial conditions during the early acoustic transients and the disagreement between different initial conditions is to be expected.

References

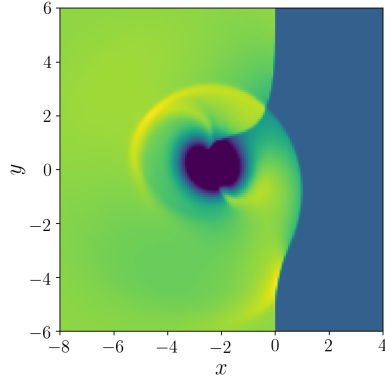
References

- [1] P. Batten, N. Clarke, C. Lambert, and D. Causon. On the choice of wavespeeds for the HLLC Riemann solver. *SIAM Journal on Scientific Computing*, 18(6):1553–1570, 1997.
- [2] A. Bhagatwala and S. K. Lele. A modified artificial viscosity approach for compressible turbulence simulations. *Journal of Computational Physics*, 228(14):4965–4969, 2009.
- [3] R. Borges, M. Carmona, B. Costa, and W. S. Don. An improved weighted essentially non-oscillatory scheme for hyperbolic conservation laws. *Journal of Computational Physics*, 227(6):3191–3211, 2008.
- [4] M. E. Brachet, D. I. Meiron, S. A. Orszag, B. Nickel, R. H. Morf, and U. Frisch. Small-scale structure of the Taylor–Green vortex. *Journal of Fluid Mechanics*, 130:411–452, 1983.
- [5] A. Chatterjee and S. Vijayaraj. Multiple sound generation in interaction of shock wave with strong vortex. *AIAA journal*, 46(10):2558–2567, 2008.
- [6] A. W. Cook. Artificial fluid properties for large-eddy simulation of compressible turbulent mixing. *Physics of Fluids (1994-present)*, 19(5):055103, 2007.
- [7] A. W. Cook and W. H. Cabot. A high-wavenumber viscosity for high-resolution numerical methods. *Journal of Computational Physics*, 195(2):594–601, 2004.
- [8] A. W. Cook and W. H. Cabot. Hyperviscosity for shock-turbulence interactions. *Journal of Computational Physics*, 203(2):379–385, 2005.
- [9] X. Deng and H. Zhang. Developing high-order weighted compact nonlinear schemes. *Journal of Computational Physics*, 165(1):22–44, 2000.
- [10] B. Einfeldt, C.-D. Munz, P. L. Roe, and B. Sjögreen. On Godunov-type methods near low densities. *Journal of Computational Physics*, 92(2):273–295, 1991.

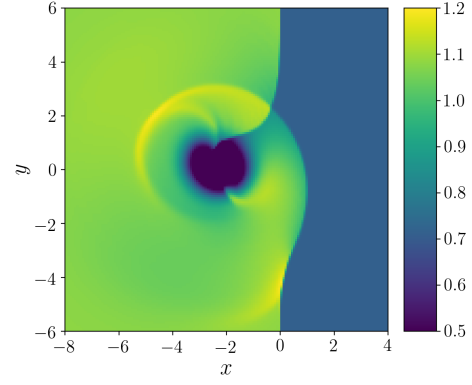
⁷Through private communication, 2018

- [11] L. Fu, X. Hu, and N. A. Adams. A family of high-order targeted ENO schemes for compressible-fluid simulations. *Journal of Computational Physics*, 305:333–359, 2016.
- [12] L. Fu, X. Hu, and N. A. Adams. Targeted ENO schemes with tailored resolution property for hyperbolic conservation laws. *Journal of Computational Physics*, 349:97–121, 2017.
- [13] N. S. Ghaisas, A. Subramaniam, and S. K. Lele. A unified high-order Eulerian method for continuum simulations of fluid flow and of elastic-plastic deformations in solids. *Journal of Computational Physics*, 371:452–482, 2018.
- [14] D. Ghosh and J. D. Baeder. Compact reconstruction schemes with weighted ENO limiting for hyperbolic conservation laws. *SIAM Journal on Scientific Computing*, 34(3):A1678–A1706, 2012.
- [15] V. Granet, O. Vermorel, T. Léonard, L. Gicquel, and T. Poinso. Comparison of nonreflecting outlet boundary conditions for compressible solvers on unstructured grids. *AIAA journal*, 48(10):2348–2364, 2010.
- [16] A. Harten, P. D. Lax, and B. v. Leer. On upstream differencing and Godunov-type schemes for hyperbolic conservation laws. *SIAM Review*, 25(1):35–61, 1983.
- [17] A. K. Henrick, T. D. Aslam, and J. M. Powers. Mapped weighted essentially non-oscillatory schemes: achieving optimal order near critical points. *Journal of Computational Physics*, 207(2):542–567, 2005.
- [18] X. Hu and N. Adams. Scale separation for implicit large eddy simulation. *Journal of Computational Physics*, 230(19):7240–7249, 2011.
- [19] X. Hu, Q. Wang, and N. Adams. An adaptive central-upwind weighted essentially non-oscillatory scheme. *Journal of Computational Physics*, 229(23):8952–8965, 2010.
- [20] X. Hu, N. A. Adams, and C.-W. Shu. Positivity-preserving method for high-order conservative schemes solving compressible Euler equations. *Journal of Computational Physics*, 242:169–180, 2013.
- [21] K. Huang, H. Wu, H. Yu, and D. Yan. Cures for numerical shock instability in HLLC solver. *International Journal for Numerical Methods in Fluids*, 65(9):1026–1038, 2011.
- [22] O. Inoue and Y. Hattori. Sound generation by shock-vortex interactions. *Journal of Fluid Mechanics*, 380:81–116, 1999.
- [23] G.-S. Jiang and C.-W. Shu. Efficient implementation of weighted ENO schemes. Technical report, DTIC Document, 1995.
- [24] E. Johnsen, J. Larsson, A. V. Bhagatwala, W. H. Cabot, P. Moin, B. J. Olson, P. S. Rawat, S. K. Shankar, B. Sjögren, H. C. Yee, X. Zhong, and S. K. Lele. Assessment of high-resolution methods for numerical simulations of compressible turbulence with shock waves. *Journal of Computational Physics*, 229(4):1213–1237, 2010.
- [25] S. Kawai, S. K. Shankar, and S. K. Lele. Assessment of localized artificial diffusivity scheme for large-eddy simulation of compressible turbulent flows. *Journal of Computational Physics*, 229(5):1739–1762, 2010.
- [26] J. Larsson, S. Lele, and P. Moin. Effect of numerical dissipation on the predicted spectra for compressible turbulence. In *Annual Research Briefs*, pages 45–57. Center for Turbulence Research, Stanford University, 2007.
- [27] S. Lee, S. K. Lele, and P. Moin. Eddy shocklets in decaying compressible turbulence. *Physics of Fluids A: Fluid Dynamics*, 3(4):657–664, 1991.
- [28] S. K. Lele. Compact finite difference schemes with spectral-like resolution. *Journal of Computational Physics*, 103(1):16–42, 1992.
- [29] X. Liu, S. Zhang, H. Zhang, and C.-W. Shu. A new class of central compact schemes with spectral-like resolution II: Hybrid weighted nonlinear schemes. *Journal of Computational Physics*, 284:133–154, 2015.
- [30] M. P. Martín, E. M. Taylor, M. Wu, and V. G. Weirs. A bandwidth-optimized WENO scheme for the effective direct numerical simulation of compressible turbulence. *Journal of Computational Physics*, 220(1):270–289, 2006.
- [31] E. Motheau, A. Almgren, and J. B. Bell. Navier–Stokes characteristic boundary conditions using ghost cells. *AIAA Journal*, pages 1–10, 2017.
- [32] S. Nagarajan, S. K. Lele, and J. H. Ferziger. A robust high-order compact method for large eddy simulation. *Journal of Computational Physics*, 191(2):392–419, 2003.
- [33] S. N. Nguechue and S. Abelman. A computational algorithm for solving nearly penta-diagonal linear systems. *Applied Mathematics and Computation*, 203(2):629–634, 2008.
- [34] T. Nonomura and K. Fujii. Effects of difference scheme type in high-order weighted compact nonlinear schemes. *Journal of Computational Physics*, 228(10):3533–3539, 2009.
- [35] T. Nonomura and K. Fujii. Robust explicit formulation of weighted compact nonlinear scheme.

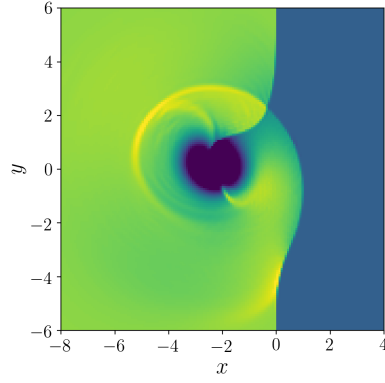
- Computers & Fluids*, 2013.
- [36] T. Nonomura, N. Iizuka, and K. Fujii. Increasing order of accuracy of weighted compact nonlinear scheme. *AIAA Paper*, 893, 2007.
 - [37] S. Pirozzoli. On the spectral properties of shock-capturing schemes. *Journal of Computational Physics*, 219(2):489–497, 2006.
 - [38] S. Pirozzoli. Generalized conservative approximations of split convective derivative operators. *Journal of Computational Physics*, 229(19):7180–7190, 2010.
 - [39] L. I. Sedov. *Similarity and dimensional methods in mechanics*. CRC press, 1993.
 - [40] S. Shankar, S. Kawai, and S. Lele. Numerical simulation of multicomponent shock accelerated flows and mixing using localized artificial diffusivity method. In *48th AIAA Aerospace Sciences Meeting Including the New Horizons Forum and Aerospace Exposition*, page 352, 2010.
 - [41] C.-W. Shu and S. Osher. Efficient implementation of essentially non-oscillatory shock-capturing schemes. *Journal of Computational Physics*, 77(2):439–471, 1988.
 - [42] G. A. Sod. A survey of several finite difference methods for systems of nonlinear hyperbolic conservation laws. *Journal of Computational Physics*, 27(1):1–31, 1978.
 - [43] R. J. Spiteri and S. J. Ruuth. A new class of optimal high-order strong-stability-preserving time discretization methods. *SIAM Journal on Numerical Analysis*, 40(2):469–491, 2002.
 - [44] A. Subramaniam, N. S. Ghaisas, and S. K. Lele. High-order Eulerian simulations of multimaterial elastic-plastic flow. *Journal of Fluids Engineering*, 140(5):050904, 2018.
 - [45] M. L. Wong and S. K. Lele. High-order localized dissipation weighted compact nonlinear scheme for shock-and interface-capturing in compressible flows. *Journal of Computational Physics*, 339:179–209, 2017.
 - [46] P. Woodward and P. Colella. The numerical simulation of two-dimensional fluid flow with strong shocks. *Journal of Computational Physics*, 54(1):115–173, 1984.
 - [47] S. Zhang, Y.-T. Zhang, and C.-W. Shu. Multistage interaction of a shock wave and a strong vortex. *Physics of Fluids (1994-present)*, 17(11):116101, 2005.
 - [48] S. Zhang, S. Jiang, and C.-W. Shu. Development of nonlinear weighted compact schemes with increasingly higher order accuracy. *Journal of Computational Physics*, 227(15):7294–7321, 2008.
 - [49] X. Zhang and C.-W. Shu. Positivity-preserving high order finite difference WENO schemes for compressible euler equations. *Journal of Computational Physics*, 231(5):2245–2258, 2012.



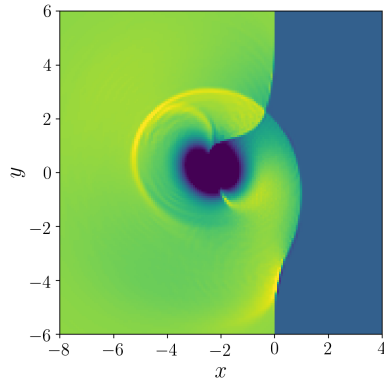
(a) WCNS5-JS



(b) WCNS5-Z

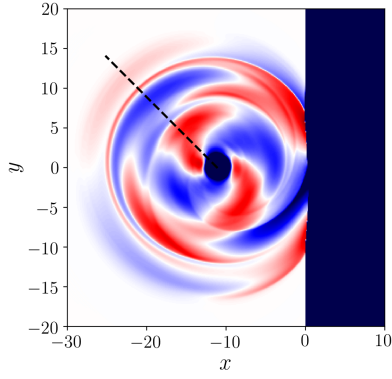


(c) WCNS6-LD

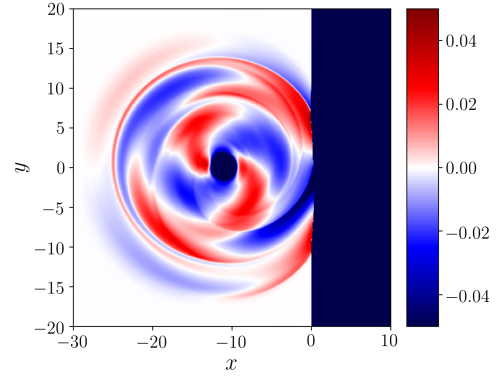


(d) WCHR6

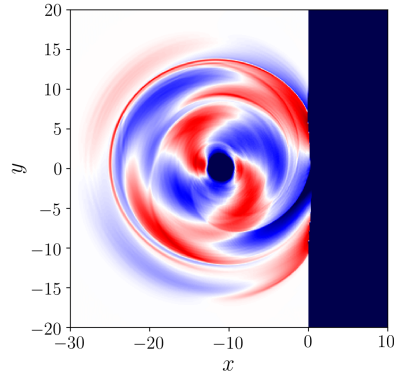
Figure 24: Pressure fields for the shock-vortex interaction problem on a 512×512 grid at $t = 6$.



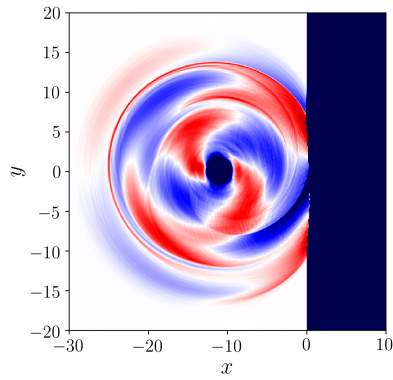
(a) WCNS5-JS



(b) WCNS5-Z

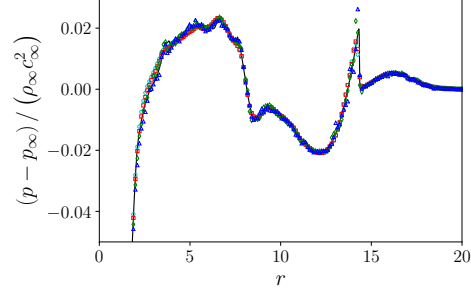


(c) WCNS6-LD

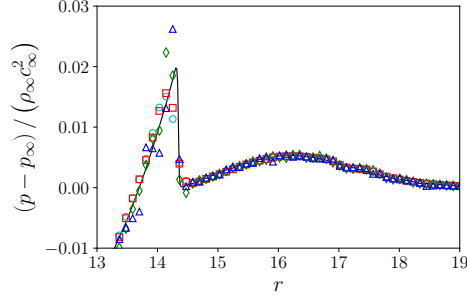


(d) WCHR6

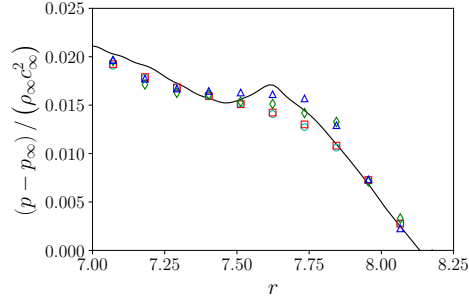
Figure 25: Sound pressure fields defined by $(p - p_\infty) / (\rho_\infty c_\infty^2)$ for the shock-vortex interaction problem on a 512×512 grid at $t = 16$. The black dashed line in (a) shows the line used to get the radial sound pressure profile plotted in figure 26.



(a) Global profile

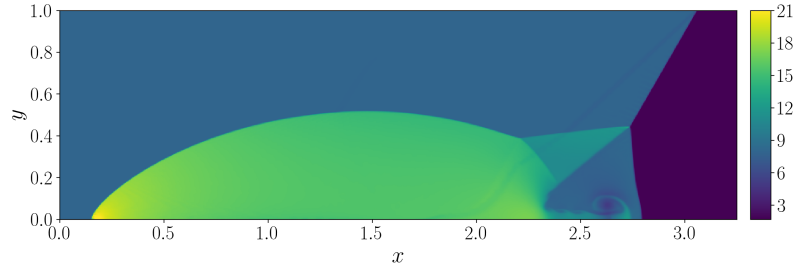


(b) Local profile 1

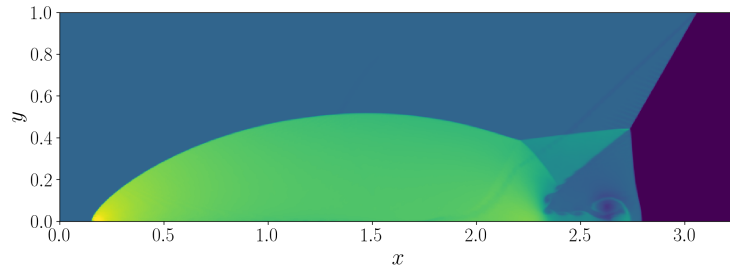


(c) Local profile 2

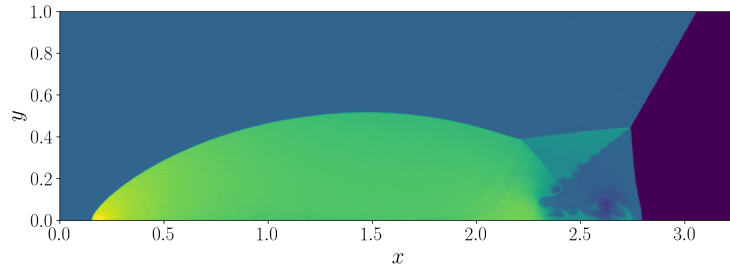
Figure 26: Sound pressure defined by $(p - p_\infty) / (\rho_\infty c_\infty^2)$ for the shock vortex interaction problem at $t = 16$ on a radial line centered at the vortex core with $\theta = -45^\circ$ as indicated by the black dashed line in figure 25(a). Black solid line: reference; cyan circles: WCNS5-JS; red squares: WCNS5-Z; green diamonds: WCNS6-LD; blue triangles: WCHR6.



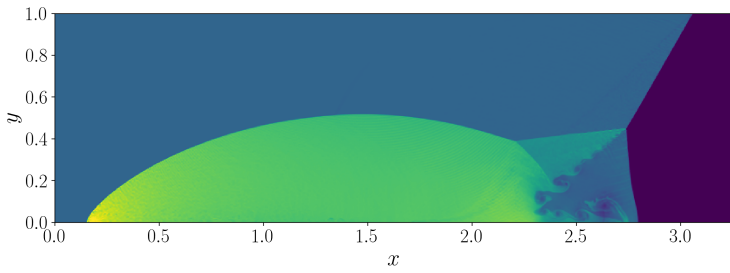
(a) WCNS5-JS



(b) WCNS5-Z



(c) WCNS6-LD



(d) WCHR6

Figure 27: Density fields for the double Mach reflection problem at $t = 0.2$ using different schemes.

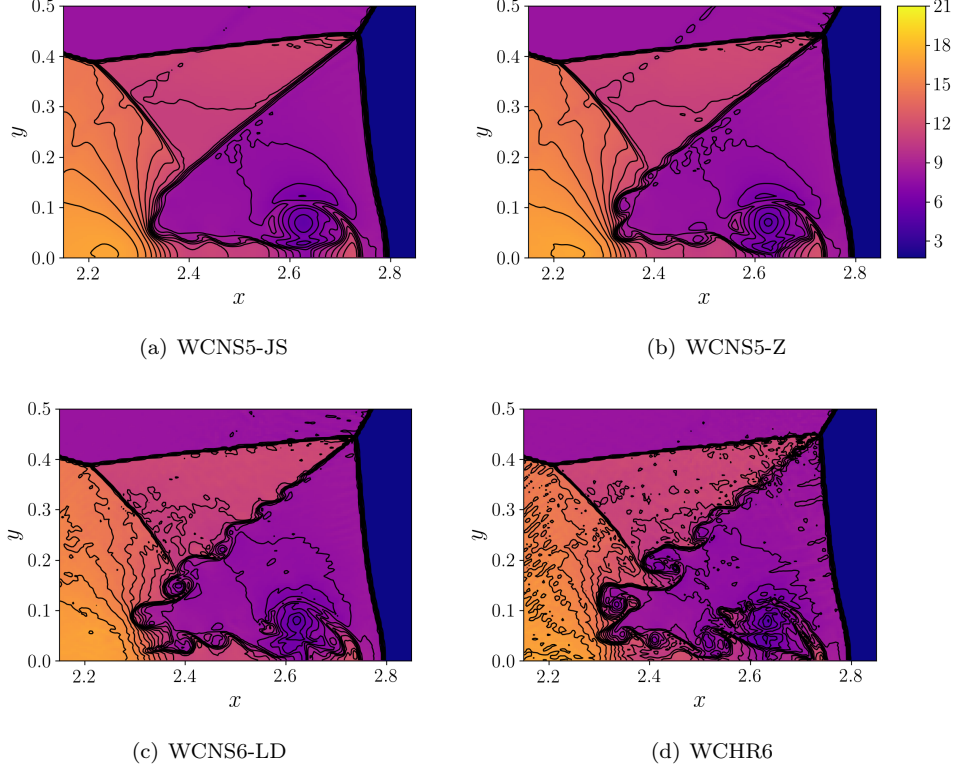


Figure 28: 30 equally spaced contours of density from 1.7 to 21 for the double Mach reflection problem at $t = 0.2$ using different schemes in the blown-up region around the Mach stem.

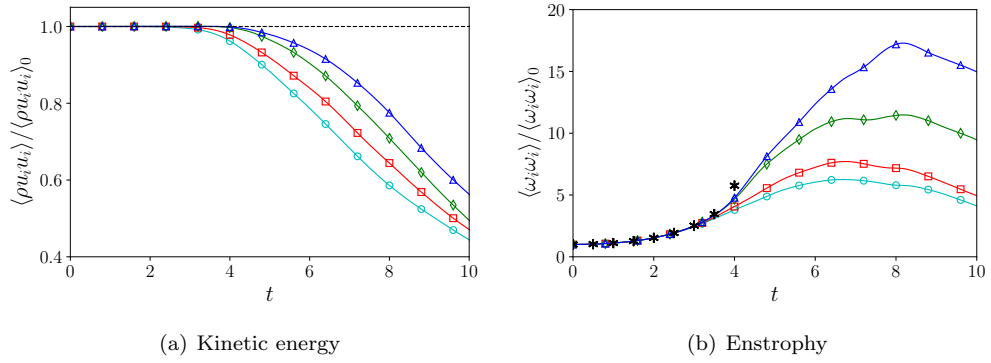
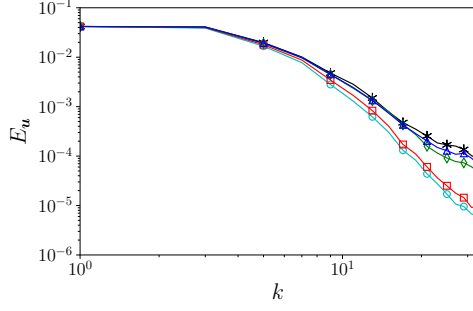
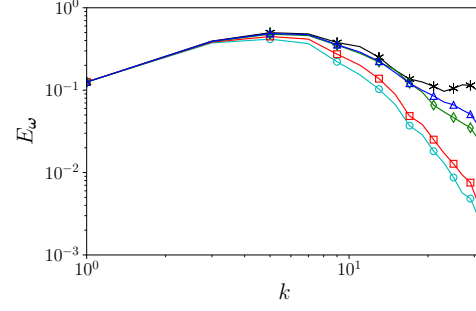


Figure 29: Time evolution of statistical quantities for the Taylor–Green vortex problem on a 64^3 grid. Black dashed line: exact for kinetic energy; black asterisks: semi-analytical result for enstrophy of Brachet et al. [4]; cyan circles: WCNS5-JS; red squares: WCNS5-Z; green diamonds: WCNS6-LD; blue triangles: WCHR6.

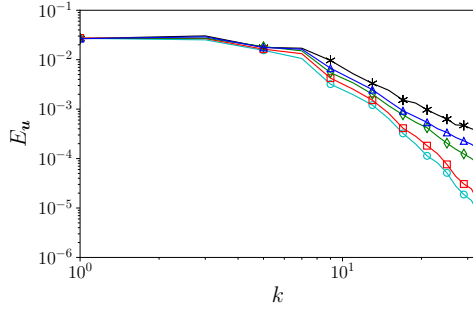


(a) Velocity energy spectrum

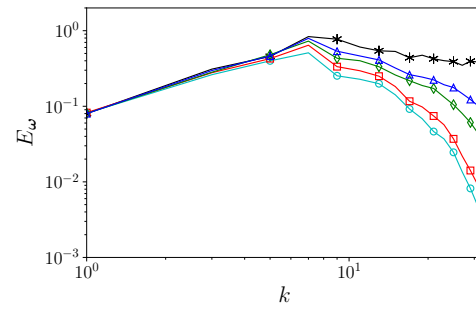


(b) Vorticity energy spectrum

Figure 30: Spectra at $t = 5$ for the Taylor–Green vortex problem on a 64^3 grid. Black asterisks: converged spectrum on a 256^3 grid of tenth order compact scheme with localized artificial dissipation; cyan circles: WCNS5-JS; red squares: WCNS5-Z; green diamonds: WCNS6-LD; blue triangles: WCHR6.



(a) Velocity energy spectrum



(b) Vorticity energy spectrum

Figure 31: Spectra at $t = 7$ for the Taylor–Green vortex problem on a 64^3 grid. Black asterisks: converged spectrum on a 256^3 grid of tenth order compact scheme with localized artificial dissipation; cyan circles: WCNS5-JS; red squares: WCNS5-Z; green diamonds: WCNS6-LD; blue triangles: WCHR6.

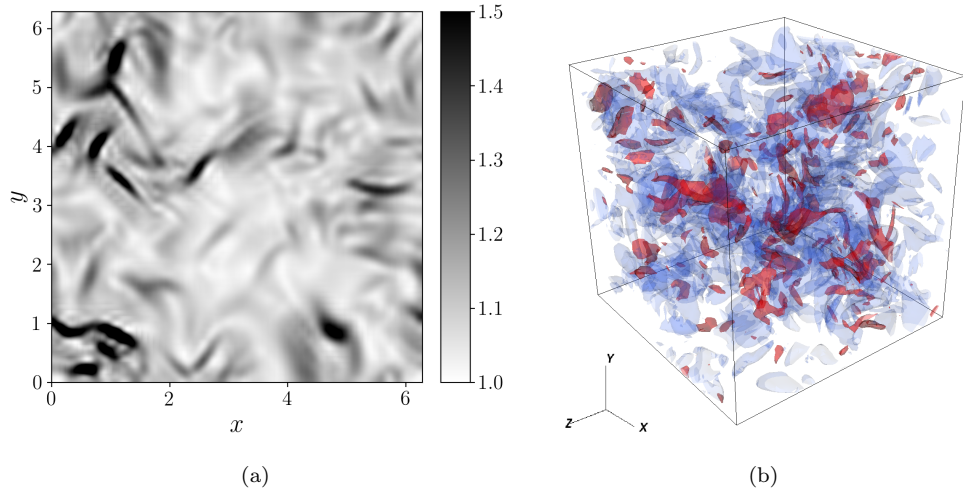


Figure 32: (a) Numerical schlieren visualized by $\exp\left(\frac{\|\nabla\rho\|}{\|\nabla\rho\|_{\max}}\right)$ on a $z = 0$ slice for the compressible homogeneous isotropic turbulence problem on a 64^3 grid at $t/\tau = 0.125$. (b) Isocontours of enstrophy at twice the mean (blue) and isocontours of dilatation at 3σ below the mean (red) for the same problem on the same grid at the same time, where σ is the standard deviation.

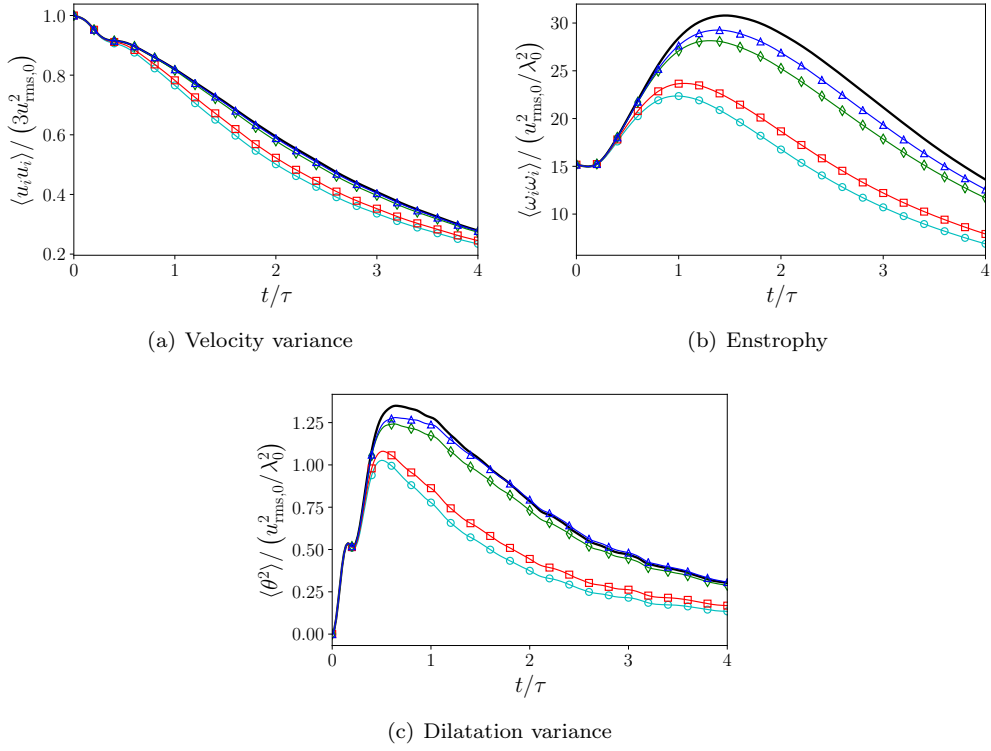


Figure 33: Time evolution of statistical quantities for the compressible homogeneous isotropic turbulence problem on a 64^3 grid with $M_t = 0.6$. Black solid line : spectrally filtered DNS; cyan circles: WCNS5-JS; red squares: WCNS5-Z; green diamonds: WCNS6-LD; blue triangles: WCHR6.

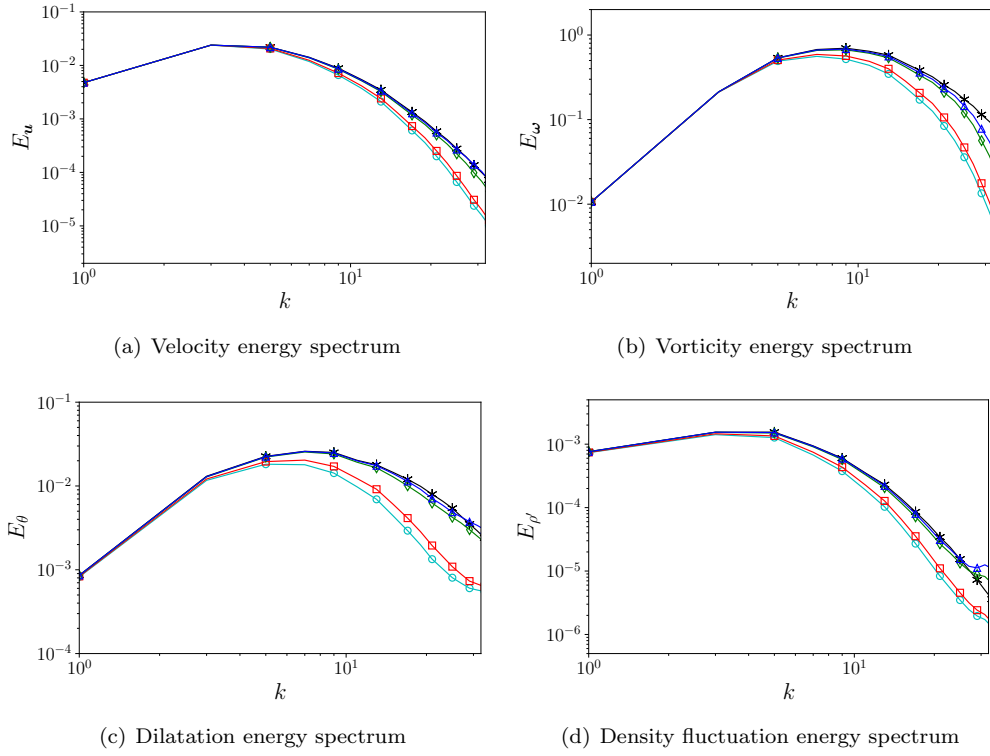
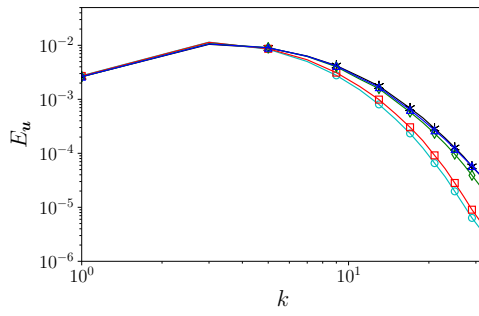
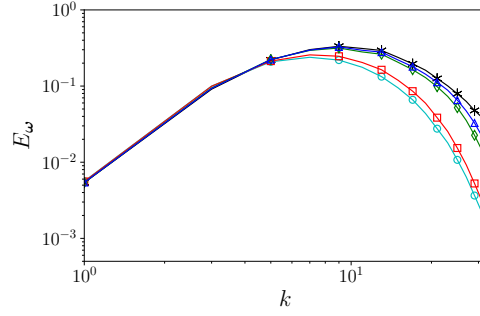


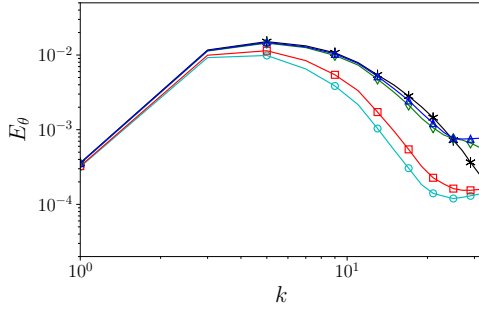
Figure 34: Spectra at $t/\tau = 2$ for the compressible homogeneous isotropic turbulence problem on a 64^3 grid with $M_t = 0.6$. Black asterisks: spectrally filtered DNS; cyan circles: WCNS5-JS; red squares: WCNS5-Z; green diamonds: WCNS6-LD; blue triangles: WCHR6.



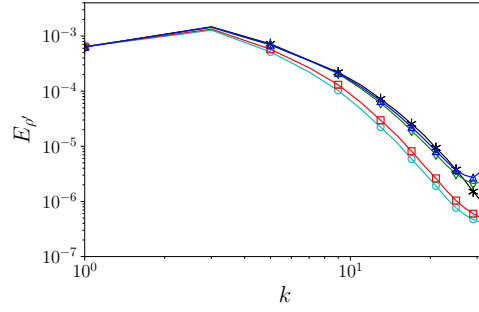
(a) Velocity energy spectrum



(b) Vorticity energy spectrum

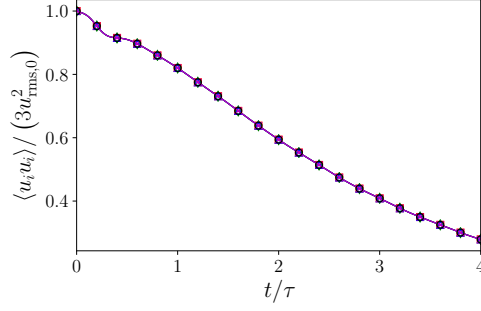


(c) Dilatation energy spectrum

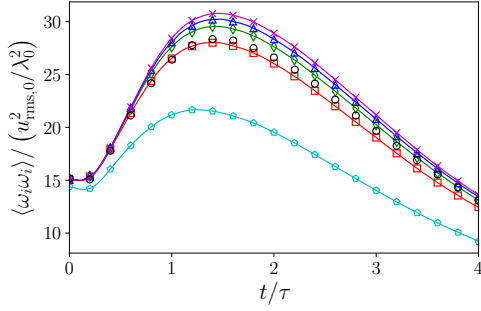


(d) Density fluctuation energy spectrum

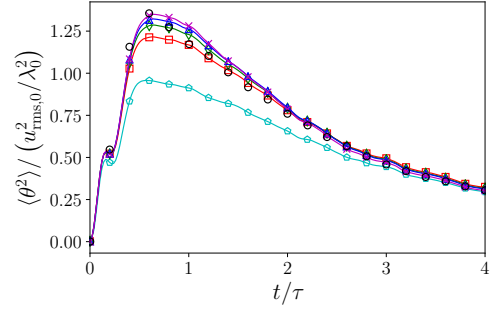
Figure 35: Spectra at $t/\tau = 4$ for the compressible homogeneous isotropic turbulence problem on a 64^3 grid with $M_t = 0.6$. Black asterisks: spectrally filtered DNS; cyan circles: WCNS5-JS; red squares: WCNS5-Z; green diamonds: WCNS6-LD; blue triangles: WCHR6.



(a) Velocity variance



(b) Enstrophy



(c) Dilatation variance

Figure F.36: Time evolution of statistical quantities for the compressible homogeneous isotropic turbulence problem presented in section 3.11 using different postprocessing derivative schemes on the DNS data. Black circles: Johnsen et al. [24]; cyan pentagons: 2nd order central explicit finite difference; red squares: 6th order central explicit finite difference; green diamonds: 6th order central compact finite difference; blue triangles: 10th order central compact finite difference; magenta crosses: spectral derivatives.